



---

# TOWARDS AN UNSUPERVISED LARGE-SCALE 2D AND 3D BUILDING MAPPING WITH AIRBORNE LIDAR DATA

---

A PREPRINT

 **Hunsoo Song**  
Lyles School of Civil Engineering  
Purdue University  
West Lafayette, IN 47907  
hunsoo@purdue.edu

 **Jinha Jung** \*  
Lyles School of Civil Engineering  
Purdue University  
West Lafayette, IN 47907  
jinha@purdue.edu

August 26, 2022

## ABSTRACT

A 2D and 3D building map provides invaluable information for understanding human activities and their impacts on the Earth and its environment. Despite enormous efforts to improve the quality of building maps, current large-scale building maps generated from automated methods have many errors and uncertainties and are often limited to providing only 2D building information. This study presents an open-source unsupervised 2D and 3D building extraction algorithm with airborne LiDAR data that is suitable for large-scale building mapping. Our algorithm operates in a fully unsupervised manner and does not require either any training label or training procedure. Our algorithm consists of simple operations of morphological filtering and planarity-based filtering. Thus, the computation is efficient, and the results are easy to predict, which can greatly reduce uncertainties in the resulting building map. A quantitative and qualitative evaluation with a large-scale dataset ( $> 550 \text{ km}^2$ ) of Denver and New York City showed that our algorithm can produce more accurate building maps than Microsoft Building Footprints which is generated by a deep learning-based method. Extensive evaluations in different conditions of landscapes confirmed that our algorithm is scalable and can be improved further with appropriate parameter selection. We also detailed the impact of parameters and potential sources of error to assist potential users of our algorithm. Our LiDAR-based algorithm has advantages in that it is computationally efficient to generate both 2D and 3D building maps, while it generates accurate and explainable results. Our proposed algorithm provides great potential towards a global-scale 2D and 3D building mapping with airborne LiDAR data.

**Keywords** Building Extraction · LiDAR · Unsupervised · 3D Building · Semantic Segmentation

## 1 Introduction

A building is a space where most of the human activities take place. Observing the formation of buildings and their spatial and structural changes provides valuable information for understanding human activities and their impact on the planet and ecosystems (Zhu et al., 2019). Particularly from a remote sensing point of view, buildings often become the smallest unit of a human-made object on Earth that can be identifiable, and they occupy the largest portion of a human-made object on Earth. Building maps generated from remotely sensed imagery have provided significant information for numerous social and environmental studies such as urban ecology (Hong et al., 2019), disaster management (Ghaffarian et al., 2019; Yeom et al., 2019), humanitarian aid (Herfort et al., 2021; Bonafilia et al., 2019), population estimation (Wu et al., 2005), and smart city planning (Herbert & Chen, 2015). Obviously, the value of the knowledge from such studies relies heavily on the accuracy of the underlying building map. However, building maps are not perfect and inherently have uncertainties and errors that propagate into downstream studies. Although these uncertainties and errors can mislead subsequent outcomes, they are hard to recognize and fix once a building map is generated. To address these

---

\*Corresponding author.

issues, the remote sensing community has been putting a lot of effort into improving the accuracy and the quality of building mapping.

With the tremendous efforts for building mapping, many building maps now exist and have become publicly available. Most of their end products are a form of 2D building map or building footprints because available data sources for building identification are mostly remotely sensed optical imagery that are often limited to providing only 2D information of buildings. OpenStreetMap (OSM) and authoritative maps are representative examples of such cases. OSM is the most popular crowdsourced map that has global-scale coverage. Any volunteers can create or edit a building instance and tag it to describe what the instance is for any area of the world using base layers available for the region, and the resulting annotations become the open building map. The OSM project started in 2004, and now it has more than 1 million users and more than 400 million building labels (Herfort et al., 2021). As it is based on the collaboration of volunteers from all around the world, its spatial coverage is the largest. However, its completeness and accuracy are still limited, and vintages of building labels are not consistent even in an adjacent area (Vargas-Munoz et al., 2020). In contrast, authoritative maps are produced by professional land surveyors typically with the request of the government. As opposed to OpenStreetMap, authoritative maps are legislated or regulated and usually certified in their accuracy so that the data can be used for the determination of property boundaries and engineering decisions. Building labels from authoritative maps are often regarded as the most accurate label or the ground-truth (Dorn et al., 2015; Mahabir et al., 2017; Jokar Arsanjani et al., 2015). However, their spatial coverage is much more limited than that of OpenStreetMap, as producing an authoritative map is expensive. In short, publicly open building maps have a trade-off between their spatial coverage and their accuracy as generating building labels entails time-consuming and labor-intensive costs.

To reduce the cost, a lot of research has been done to develop algorithms that can automatically generate building maps. Most significant advancements in recent years were made with several contests and the development of deep learning algorithms. One of the earliest contests was held by the International Society for Photogrammetry and Remote Sensing (ISPRS) community (Rottensteiner et al., 2012, 2014). By providing both optical images and a digital surface model (DSM) on several cities, they held a contest to accurately map the semantic label of land use map including a building class. Lots of algorithms were developed for the contest, and they showed reasonable accuracy for automatic building map generation. Particularly, top performers of the contest were able to produce reliable building maps having only a marginal error (Rottensteiner et al., 2014). However, as the study areas were limited in their spatial coverage (less than 10 km<sup>2</sup> in total)<sup>1</sup>, they do not cover different types of buildings placed in diverse environments. Therefore, it is hard to claim that developed algorithms in the specific study area will work well for other diverse landscapes.

More recently, with the advancement of deep learning technology, several contests were held for semantic segmentation of building with a much larger dataset. One notable challenge was SpaceNet (Van Etten et al., 2018). The dataset covers around 6,000 km<sup>2</sup> with less than 1-meter resolution of satellite images over several countries and includes more than three hundred thousand building labels. In this challenge, deep learning-based algorithms have shown the highest accuracy. Since this challenge, deep learning-based algorithms have been dominating literature for the automatic generation of building footprints (Yuan et al., 2021b; Ma et al., 2019; Zhu et al., 2017). However, their accuracies vary considerably depending on the region and the training condition (Yang et al., 2018; Kaiser et al., 2017). This is because learning-based algorithms are always biased towards the distribution of available training data and are likely to perform poorly when encountering out-of-distribution data (Moreno-Torres et al., 2012). Although lots of efforts, namely, transfer learning (Maggiori et al., 2016) and domain adaptation (Deng et al., 2019; Makkar et al., 2021), have been going on for addressing the problem of distribution shift, the reuse of a pre-trained model for different study areas or the development of a model that can be universally applicable is a very challenging problem.

One milestone in a large-scale building map was Microsoft Building Footprints (MBF)<sup>2</sup>. Microsoft Building Footprints released the largest building footprints that were generated by a machine. They have released country-wide open building footprints datasets, including the US, Canada, Australia, and several countries in South America and Africa. More than 200 million building labels were currently annotated (August 2022). A deep learning model called EfficientNet (Tan & Le, 2019) was trained with millions of building labels and their corresponding satellite images, and the outputs of the model were refined based on a polygonization algorithm to produce the final building footprint maps. The MBF is a significant accomplishment in that it provides the first continental-level open building maps generated by algorithms. However, similar to the OpenStreetMap, it contains many errors, and its quality is not consistent as diverse optical images with different atmospheric conditions were used for the mapping (Heris et al., 2020). Considering the fact that the machine-generated building map is still not accurate enough to replace the authoritative maps, even with the use of millions of satellite images and their corresponding labels, we can argue that a deep learning-based building extraction using optical imagery needs another breakthrough to close the accuracy gap between machine-generated maps and authoritative maps. Moreover, for regions where available training labels and images are scarce, and their

<sup>1</sup><https://www.isprs.org/education/benchmarks/UrbanSemLab/semantic-labeling.aspx>

<sup>2</sup><https://www.microsoft.com/en-us/maps/building-footprints>

building appearance are fairly different, such as slums or under-developed countries, attaining satisfactory results with a supervised algorithm would become more challenging (Wurm et al., 2019; Williams et al., 2019).

Even putting the accuracy of the building footprint map aside from our discussion, a building cannot be fully characterized in a 2D space. Essentially, buildings are 3D objects. Urban expansion is not just occurring within a 2D space but also in a 3D space. As cities become denser and taller, understanding buildings from a 3D perspective is becoming more crucial. This is because 2D building maps become more different from the actual 3D building shape. As 2D and 3D representations of the building become more unlike, 2D building map would not fully explain their role and their impacts on environments (Li et al., 2020; Herbert & Chen, 2015). In other words, studies based on 2D building maps could lead to a biased result, particularly if what one really needed was a building volume, not a building area. To name a few examples, an urban heat island analysis (Park et al., 2021; Yu et al., 2021; Huang & Wang, 2019) and a population estimation Wang et al. (2016); Biljecki et al. (2016a) would be more accurate with 3D building data. 3D building map will not only provide richer information for downstream analyses Biljecki et al. (2016b) but also it will accelerate new research, including urban air mobility navigations Kim & Yoon (2021); Bauranov & Rakas (2021), digital twin simulations (Lehner & Dorffner, 2020; White et al., 2021), and other diverse smart city applications (Han et al., 2022; Macchione et al., 2019; Zhou et al., 2019).

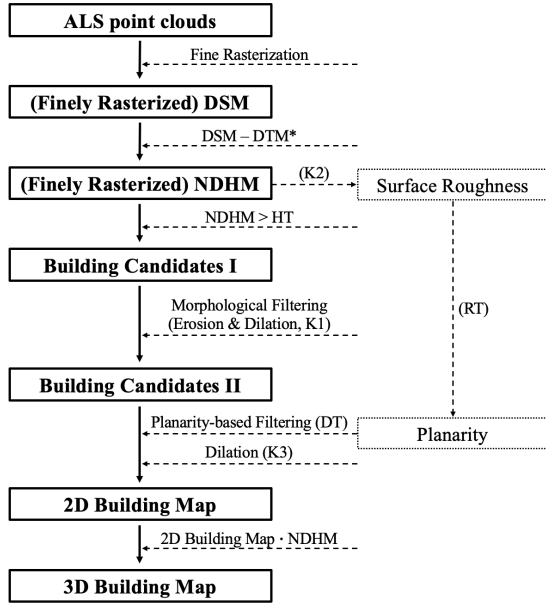
Airborne laser scanning (ALS) is known to be the most robust and efficient method for collecting 3D information about buildings when point density is good enough. There have been numerous efforts for the 3D characterization of building from optical sensors (Cheng et al., 2011, 2013; Hu et al., 2021; Huang et al., 2022; Qin, 2019) or SAR sensors (Li et al., 2020; Domínguez et al., 2019). However, they either require a lot of satellite images meeting particular conditions and are limited in their performances to generate detailed 3D information. When it comes to 2D building mapping, the biggest drawback of LiDAR lies in its cost compared with that of the optical sensor. In terms of the cost of data collection, this is true in general. However, if the generation of 3D building information is needed or if LiDAR-based building mapping can produce a more accurate 2D building map than other sensors, LiDAR could be a good alternative for both 2D and 3D building mappings. In addition, the current state-of-the-art methods for automatic building mapping based on optical images require heavy computation and big training samples that are expensive (Yang et al., 2018; Van Etten et al., 2018). Needless to say, if the target is to generate a 3D building map, the overall project cost may increase significantly, and it is often next to impossible. Therefore, if a new framework to generate 2D and 3D building maps from LiDAR data is developed, LiDAR-based building mapping can be more attractive than other methods in both accuracy and cost.

This paper presents a fully automatic algorithm to produce 2D and 3D building maps from airborne LiDAR data. Our method operates in an unsupervised manner, so it does not require any training labels. Only discrete point cloud data from a typical topography ALS are needed for generating 2D and 3D building maps. Our algorithm extracts buildings based on the physical properties of buildings that buildings are laser-impermeable and relatively smooth ground-standing objects. To be more specific, our method uses morphological filtering and planarity-based filtering in a finely rasterized representation of LiDAR data. The generated 2D building map was quantitatively evaluated in 550 km<sup>2</sup> of urban areas compared with the authoritative map and Microsoft Building Footprints. To compare different large-scale building maps effectively, a tiling comparison method that evaluates maps based on ranking after tiling them into small tiles is introduced. Also, extensive qualitative evaluations were made in diverse areas of the US to explore potential error sources of our algorithm and to validate the scalability of our algorithm for global-scale mapping.

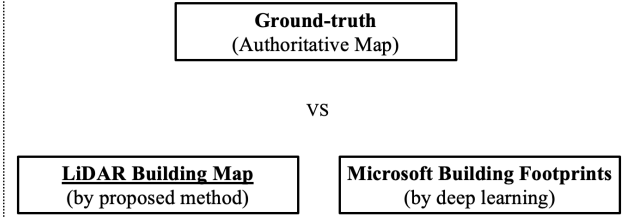
The main contributions of our study can be summarized as follows.

- We present an open-source unsupervised algorithm that can effectively generate large-scale 2D and 3D building maps using airborne LiDAR data.
- The generated 2D and 3D building maps were compared with Microsoft Building Footprints and authoritative maps in an urban area of 550 km<sup>2</sup> using a tiling comparison method.
- A quantitative and qualitative evaluation with extensive, diverse landscapes showed that our algorithm can produce more accurate building maps than Microsoft Building Footprints.
- The impact of parameter selection and potential sources of error are detailed to assist potential users of our algorithm to generate explainable, large-scale building maps.
- We identify the great potential of LiDAR-based building mapping over image-based building mapping.

The remainder of this paper is organized as follows. Section 2 introduces the proposed 2D and 3D building mapping algorithm and evaluation methods. Section 3 illustrates experimental results and analyzes the errors. Section 4 discusses the impact of parameter selections, the limitations of our study, and the potential of our method for global-scale mapping. Section 5 concludes the study.

**The Proposed 2D and 3D Building Mapping Algorithm**

DTM\*: Song & Jung (2022)  
 K1, K2, K3, HT, RT, DT: parameters

**Evaluation Methods****Dataset**

- Denver & New York City (> 550 sqkm)

**Evaluation and Analysis**

- Conventional Quantitative Evaluation
- Tiling Comparison Evaluation
- Error Analysis (detection, commission rates according to building area)

Figure 1: Overview of the methodology

## 2 Methodology

### 2.1 Overview

In this Section, we present a simple but effective algorithm for generating large-scale 2D and 3D building maps. The proposed algorithm extracts buildings from the raw ALS point clouds by exploiting the physical properties of buildings, which are ground-standing and have laser-impermeable, relatively smooth surfaces. Generated building maps by our proposed method were quantitatively and qualitatively evaluated with both conventional and tiling comparison evaluation methods for two large urban areas, Denver and New York City, covering more than 550 km<sup>2</sup> in total. Then, to investigate the strengths and weaknesses of our algorithm, detailed error analyses were made based on diverse criteria. The following subsections will illustrate the proposed building map generation algorithm and detailed descriptions of evaluation methods. Figure 1 provides an overview of the methodology section, illustrating the workflow of the proposed 2D and 3D building mapping algorithm and the summary of evaluation methods.

### 2.2 The proposed 2D and 3D building mapping algorithm

#### 2.2.1 Finely rasterized DSM generation

Our algorithm starts from the raw point cloud collected from a typical ALS system. The point cloud represents 3D coordinates of data points that are measured from the airborne LiDAR sensor. Since the observed data point is a subset of the points on the earth's surface, it necessarily has a limitation in representing the earth perfectly. The point observation can be too sparse, and the point spacing inevitably varies due to many factors such as flight configuration and the laser reflectivity of objects on the ground. To handle this irregularly spaced raw data, the raw point cloud is commonly transformed into a gridded format, called the digital surface model (DSM). During the transformation, depending on the ground sampling distance (GSD) of the DSM, the void grid where the LiDAR point does not register can occur.

The conventional way to avoid this void grid is to use a coarser GSD so that majority of grids will have at least a LiDAR point registered and to take a representative height value among points in the grid (Hyypya et al., 2001; Zhao, 2013;



Jung et al., 2014; Maltezos et al., 2018; Oh et al., 2022). Also, having multiple points in one grid enables deriving additional features to DSM (Ekhtari et al., 2008; Zhao, 2013; Maltezos et al., 2018). Studies (Awrangjeb et al., 2012; Huang et al., 2019; Chen et al., 2020) using both LiDAR and optical imagery usually generated DSM that has the same resolution of corresponding optical imagery regardless of the point density. Occasionally, how to create and rasterize a DSM from LiDAR has not been explicitly mentioned in the previous literature (Zhao et al., 2016; Yan et al., 2017; Hosseinpour et al., 2022; Yuan et al., 2021a) because it is often not considered a critical issue, or even if it is mentioned, they simply provide the software used to create the DSM (e.g. LasTools, ArcGIS)(Hosseinpour et al., 2022; Ojogbane et al., 2021). However, creating a DSM of coarse grid ("coarse rasterization") has two main problems. First, it can cause data loss. Second, it can make the differentiation between buildings and trees more difficult as it may lose the feature that can be obtained from the characteristics of laser penetration.

Instead of coarse rasterization, our algorithm uses a "fine rasterization" for generating DSM. Fine rasterization is a method that projects a point cloud into finely rasterized grids to reduce cases where multiple LiDAR points occupy a common grid. Then, it interpolates void grids. Before the interpolation, fine rasterization will obviously have more void grids than coarse rasterization and will include non-observed values, which are created data by the interpolation. However, it can prevent data loss that occurs when multiple LiDAR points are registered to the same grid. Also, the interpolation can reasonably extend the observation unless point density is severely irregular (Morgan & Habib, 2002). Specifically, the LiDAR point whose elevation is the lowest (the last return of LiDAR points) was chosen as the value for the DSM when multiple points occupy the same grid in fine rasterization. This increases the chance of collecting the penetrated laser points under the trees, and subsequently, penetrated laser points make the differentiation between buildings and trees easier. For the interpolation, the nearest interpolation is adopted in the current implementation as it can prevent distortion of height values at building boundaries.

Figure 2 emphasizes how DSM can be different depending on the rasterization method. The area shown in this figure is a sample from New Orleans, Louisiana, US, where overhanging dense trees often cover residential buildings. The area of the top figure is 0.65 km by 0.30km, and the bottom figure shows the zoomed-in area of the top figure. The laser scanning was conducted with Riegl LMS-Q680i and Riegl LMS-Q780 system, and the point density is approximately 4-points/m<sup>2</sup>. The RGB satellite image (Figure 2(a)) is from Google Earth. Figure 2(b) shows LiDAR point occupancy, which displays the grid occupied by LiDAR points in white, otherwise black. As the LiDAR point occupancy has the same GSD (0.5-meter) of fine rasterization, the black grids in LiDAR point occupancy shows void grids of DSM with fine rasterization before the interpolation. The two different DSMs created with coarse rasterization and fine rasterization are shown in Figure 2(c) and Figure 2(d), respectively. The DSM with coarse rasterization took the highest elevation when multiple points coexist in the same grid while the DSM with fine rasterization took the lowest elevation. The GSD of the coarsely rasterized DSM and the finely rasterized DSM are 2-meter and 0.5-meter, respectively. As shown in Figure 2(c), coarse rasterization can better prevent void grids, but it caused more data loss and made it difficult to distinguish between buildings and trees. On the contrary, in DSM with fine rasterization (Figure 2(d)), building objects can better retain their shapes while trees are illustrated as scattered points, which stands out the difference between buildings and trees becomes clearer. In other words, fine rasterization dramatizes the difference between the penetration properties of buildings and trees.

### 2.2.2 Finely rasterized NDHM generation

A building can be characterized as an object that stands on the ground, which means buildings are relatively tall and have a discrete height difference from the nearby ground. Therefore, simply calculating the relative height above the nearby ground and masking with a certain height elevation can effectively extract building candidates. For this, the generation of the digital terrain model (DTM), the map describing the ground elevation, must precede to generate a normalized digital height model (NDHM). The NDHM is the surface model that represents the height above the ground, and it can be produced by subtracting DTM from DSM. In our experiment, we used a finely rasterized DSM and a DTM generated with the method developed by (Song & Jung, 2022) for generating a finely rasterized NDHM. This is because the DTM generation method of (Song & Jung, 2022) considers bridges and overpasses as a ground. Otherwise, grounds under bridges and overpasses become their DEM, which will convert bridges and overpasses into building candidates since their patterns in NDHM will become similar to that of buildings (Song & Jung, 2022; Chen et al., 2017; Zhang et al., 2016). Also, since the DTM generation method (Song & Jung, 2022) has a function to classify water bodies, the classified water bodies were masked out from the building candidates in our algorithm.

### 2.2.3 2D and 3D building mapping

A visualized procedure of our algorithm for 2D and 3D building mapping is provided in Figure 3 along with a RGB satellite image from Google Earth Figure 3(a).

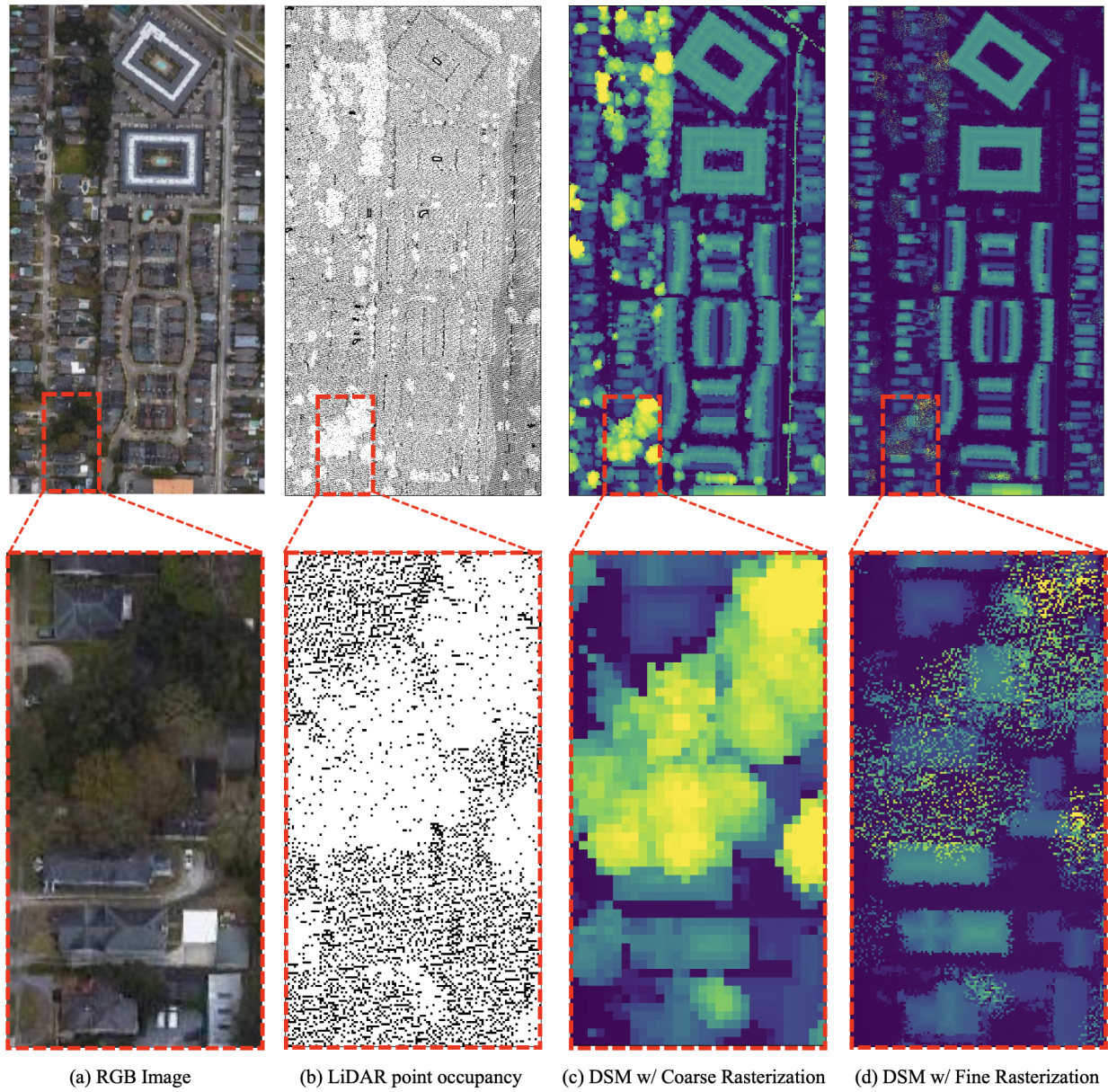


Figure 2: Comparison of two DSMs with coarse rasterization and with fine rasterization, respectively

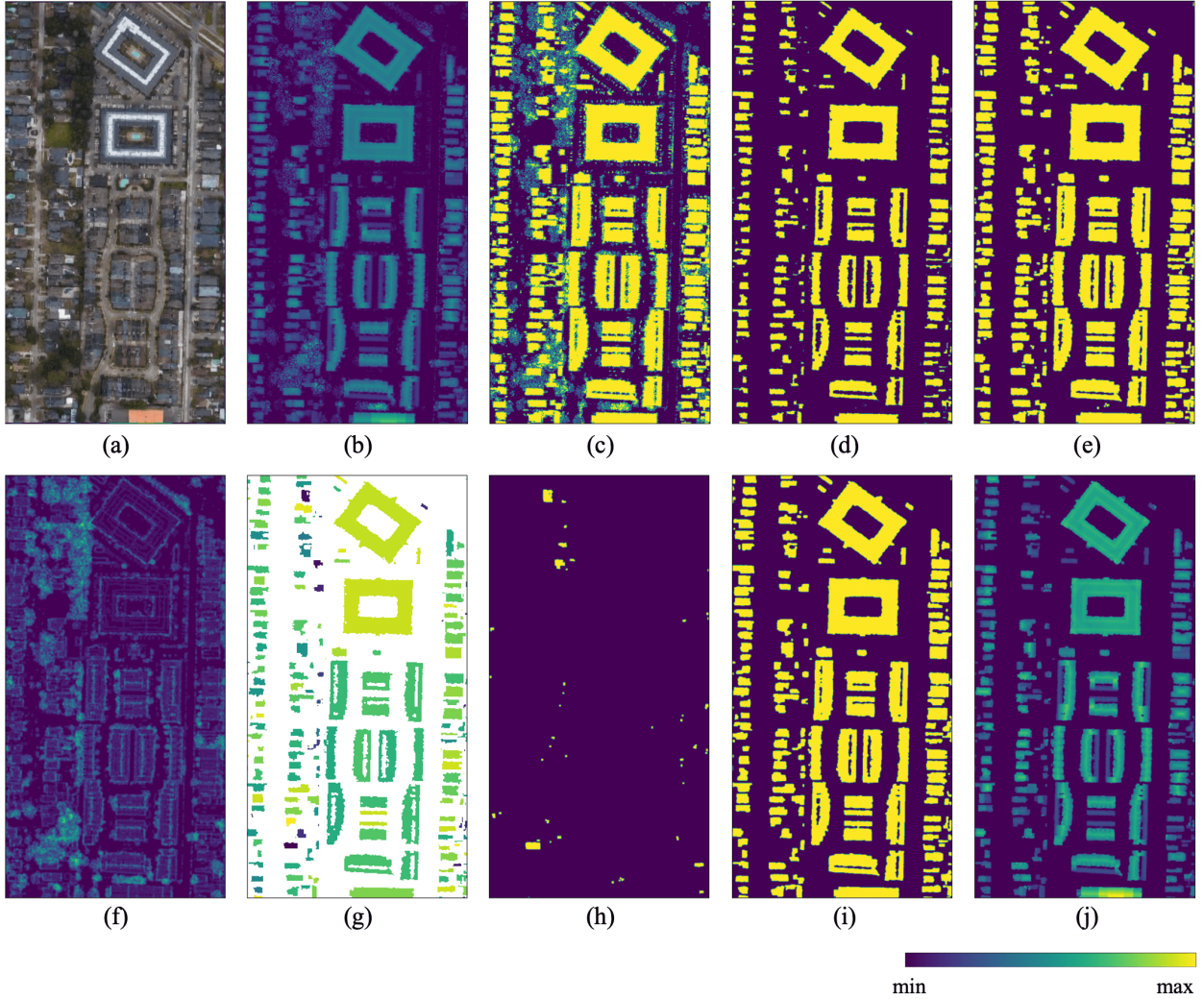


Figure 3: A visualized procedure of our algorithm: (a) RGB satellite image, (b) NDHM (0-20m), (c) NDHM > HT (0 or 1) - Building Candidates I, (d) After Erosion (0 or 1), (e) After Dilation (0 or 1) - Building Candidates II, (f) Surface Roughness (0-25), (g) Planarity (0-1), (h) Planarity < DT (0 or 1), (i) 2D Building Map (0 or 1), (j) 3D Building Map (0-20m). The color range of each image is indicated in the parentheses.

With the finely rasterized NDHM (Figure 3(b)), the building candidate map (Figure 3(c)) can be extracted by applying a mask with a certain Height Threshold (HT). The first building candidate map (Building Candidates I) will represent all objects that are relatively taller than the nearby ground as a binary format, and most of the objects in Building Candidates I will be either buildings or trees. The significant difference between buildings and trees lies in the fact that LiDAR can penetrate through trees to observe the ground under the tree (Donoghue et al., 2007; Jung et al., 2013; Oh et al., 2022), while LiDAR cannot penetrate through the building roof as its surface is solid (laser-impermeable) and flat that consistently representing higher elevation than its surrounding ground. Due to the difference in the penetration properties of buildings and trees, trees are represented like salt and pepper noise in Building Candidates I.

Next, our algorithm applies morphological filters of erosion and dilation consecutively on Building Candidates I to remove trees. The erosion filter removes small objects by eroding pixels, and the dilation filter restores the eroded pixels only if they remain after the erosion. This morphological filtering removes most of the trees as you can see in Figure 3(c)-(e) and results in the second building candidate map (Building Candidates II). As building mapping is essentially a binary classification, a trade-off between the omission and commission errors necessarily exists. When applying the morphological filter, the kernel size (K1) must be determined appropriately to consider the trade-off. If the kernel size (K1) increases, the commission error decreases as trees can be removed more aggressively after the erosion. On the other hand, the omission error increases as small buildings may be removed during the erosion process. Conversely, a



smaller kernel will increase commission errors while decreasing omission errors. The trade-off caused by the choice of  $K_1$  is analyzed in Section 4.2.1.

After applying the morphological filters, the remaining objects in Building Candidates II would be either buildings or dense trees (Figure 3(e)). Dense trees refer to trees whose leaves are so dense that LiDAR hardly penetrates through leaves. To remove the remaining dense trees, our algorithm performs planarity-based filtering based on the assumption that buildings are more planar than trees. First, to quantify the roughness of each pixel, the algorithm rounds the NDHM to have integer values and counts the number of unique integers within a square kernel ( $K_2$ ) over the NDHM. This process generates a surface roughness map (Surface Roughness, Figure 3(f)). Each pixel in Surface Roughness represents the number of unique integer values within a square window of size  $K_2$  (As  $K_2$  was set to 5, Surface Roughness has values ranging from 0 to 25). Then, the algorithm classifies a pixel as a planar pixel if its roughness value is less than a certain threshold, Roughness Threshold (RT). Let’s take an example where  $K_2$  is 5 and DT is 4. If the number of unique integer values out of 25 pixel values in a 5 by 5 window of a rounded NDHM is less than 4, the algorithm designates the center pixel of the window as a planar pixel. Lastly, the algorithm calculates the proportion of planar pixels for each remaining building candidate. The proportion is called planarity. For example, if an object in Building Candidates II consists of 100 pixels and if the number of planar pixels in the object is 20, the planarity of the candidate is 0.2. Figure 3(g) shows planarity values for every building candidate. Based on the assumption that a building roof has a more planar surface compared to dense trees, our algorithm filters out objects whose planarity values are less than a certain ratio. The certain ratio is called Dense Tree (DT), as it is a descriptor to discriminate dense trees among building candidates. Figure 3(h) shows eliminated entities with the planarity-based filtering. A more detailed description of DT is provided in Section 4.2.2. Lastly, our algorithm applies a dilation kernel of size  $K_3$  again to generate a 2D building map (Figure 3(i)). The second dilation kernel is to restore the underestimated building area because LiDAR can underestimate building boundaries. This underestimation is detailed in Section 4.2.3. Finally, the algorithm generates a 3D building map by extracting building pixels of the 2D building map from the NDHM.

In this study, we created building maps of 0.5-meter resolution and used the following default parameters. HT was set as 1.5-meter based on the assumption that buildings are taller than 1.5-meter. The kernel size ( $K_1$ ) of morphological filters was set as 7 (a 7 by 7 pixels window) for 0.5-meter resolution DSM based on the assumption that building areas are larger than 3.5-meter by 3.5-meter. A 5 by 5 pixels window was used for  $K_2$ . RT and DT were set as 4 and 0.1, respectively.  $K_3$  was set as a 5 by 5 pixels window by default. Although the best parameter combination must be different depending on the study area, we found the default parameter settings are robust in most scenarios. A more detailed discussion of parameter selection is provided in Section 4.2.

### 2.3 Evaluation methods

To quantitatively evaluate the performance of our proposed algorithm, we selected urban areas of Denver, Colorado, US (196 km<sup>2</sup>) and New York City, New York, US (357 km<sup>2</sup>) where both authoritative building maps and Microsoft Building Footprints are available. The aerial RGB imagery of two study areas are shown in Figure 4 and Figure 5, respectively. The aerial RGB imagery are from the U.S. Department of Agriculture’s (USDA) National Agriculture Imagery Program (NAIP)’s orthoimagery. Laser scanning of the Denver area was performed with the Leica TerrainMapper sensor between May and September 2020. For New York City, the Leica ALS70 sensor was used between March and April 2014. All LiDAR data used in this study are from the U.S. Geological Survey’s 3D Elevation Program (3DEP) program. The point densities of the Denver and New York City datasets are approximately 4-points/m<sup>2</sup> and 5-points/m<sup>2</sup>, respectively. Then, building maps generated by our method (“LiDAR building map”) are compared to both authoritative building maps (“ground-truth”) and Microsoft Building Footprints. All building maps were evaluated as raster with 0.5-meter resolution.

Our study area is over 550 km<sup>2</sup>. Conventionally, building extraction methods were evaluated by providing several averaged quantitative metrics such as intersection over union (IoU), precision, recall, and F1-score of entire study areas. However, as our study area is large, simply providing averaged metrics of the entire area is not sufficient to provide a detailed evaluation. Therefore, in addition to the conventional quantitative metrics, we introduced a tiling comparison method to explore the weaknesses and strengths of the proposed method in detail. The tiling comparison method is a method that compares different maps by dividing them into small tiles. The tiling comparison method has the advantage of being able to effectively show distinct differences among large-scale maps by providing a ranking of the differences. It also enables detailed comparative evaluation of algorithms whose performance may vary from region to region.

To be specific, we tiled each study area so that the area of each tile has an area of 0.5 km by 0.5 km. As a result, Denver and New York City consist of 784 tiles and 1428 tiles, respectively. With these tiles, we calculated IoUs between the LiDAR building map and Microsoft Building Footprints for every tile. Then, we ranked the IoUs to find tiles having significant differences between LiDAR building map and Microsoft Building Footprints. Based on the rank of the difference, we qualitatively compared their performances. Also, the IoU of LiDAR building map and the IoU of

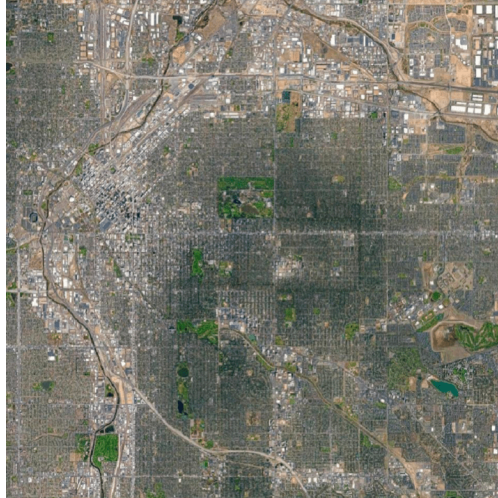


Figure 4: Study area of Denver (14-km by 14-km)

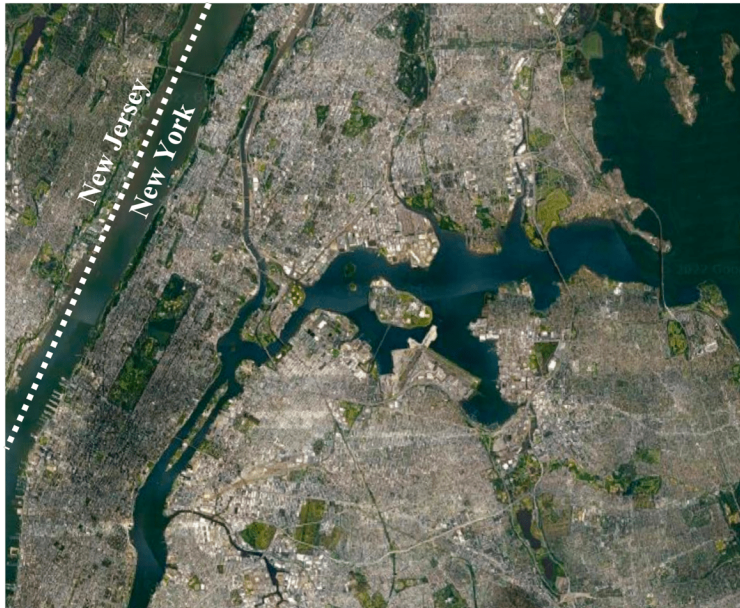


Figure 5: Study area of New York City (17-km by 21-km, New Jersey is excluded)

Microsoft Building Footprints were also calculated by comparing to the ground-truth, respectively. Lastly, we analyzed the errors of our algorithm and Microsoft’s algorithm according to the building areas.

### 3 Results

#### 3.1 Results of Denver dataset

Three building maps: LiDAR building map, Microsoft Building Footprints, and ground-truth (authoritative map) were compared using the tiling comparison method described in the previous section. For generating LiDAR building map, we used default parameter values described in Section 2.2.3. consistently for entire areas. One thing to note is that there are time discrepancies in each building map. The vintage of ground-truth for Denver is 2018, while LiDAR building map was generated with LiDAR data for 2020, and Microsoft Building Footprints were generated with optical images of 2018-2019.

### 3.1.1 Conventional quantitative results

LiDAR building map and Microsoft Building Footprints of the entire study area (196 km<sup>2</sup>) of Denver were evaluated in terms of IoU, precision, Recall, and F1-score (Table 1). As a result, LiDAR building map outperformed Microsoft Building Footprints in all metrics. IoU and recall were particularly higher than that of Microsoft Building Footprints. Considering the LiDAR building map was generated in a fully unsupervised way with a single parameter set, the result shows that our unsupervised algorithm can produce a building map more accurately than Microsoft’s supervised deep learning-based method as long as a decent quality of ALS data is available.

Table 1: Conventional quantitative results of the Denver dataset

	IoU	Precision	Recall	F1-score
LiDAR building map	<b>81.8</b>	<b>91.2</b>	<b>88.8</b>	<b>90.0</b>
Microsoft Building Footprints	77.3	90.4	84.2	87.2

### 3.1.2 Tiling evaluation

Among 784 tiles of Denver, we manually excerpted 5 tiles that rank high (top 10%) and show notable differences in building maps. Figure 6 shows RGB images and their corresponding 3D building map, LiDAR building map, Microsoft Building Footprints, and ground-truth. The RGB imagery is from NAIP’s orthoimagery. The vintage of the RGB imagery is 2015. Thus, we can expect the same buildings existing in both RGB image and LiDAR building map should also exist in Microsoft Building Footprints as the vintage of Microsoft Building Footprints (2018-2019) lies between those of RGB image (2015) and LiDAR data (2020). The ranking denoted with RGB image indicates the ranking of the largest difference between LiDAR building map and Microsoft building footprints as described in Section 2.3. The ranking is to give a sense of how significant the difference between those building maps is in the entire 784 tiles of the Denver dataset. 3D building map generated by our method are also displayed for reference with its height range. Detailed description on the quality of 3D building map is provided in Section 4.3.5. IoU values calculated by comparing LiDAR building maps and Microsoft Building Footprints respectively to ground-truth are also provided.

Buildings that led the significant difference in their performances include huge buildings and unique-shape buildings. Microsoft Building Footprints were suffering particularly for large buildings like shopping malls or warehouses as shown in the first and third rows of Figure 6. Also, buildings having unique shapes like sports complexes were not mapped properly as shown in the second and fourth rows of Figure 6. These failures in Microsoft’s algorithm can be regarded as a general limitation of deep learning-based supervised methods. Since large buildings and unique-shape buildings are not common, training samples for these kinds of buildings might not have been sufficient in the training data used to train the Microsoft’s deep model. Another possible reason for the failure of Microsoft’s algorithm could be the limited input size of image for the deep learning model. The typical input size of deep learning-based models for semantic segmentation is 256 by 256 pixels or 512 by 512 pixels. It means the model’s decision should be made by considering the limited area of 128-meter by 128-meter or 256-meter by 256-meter (assuming the resolution of the image used was 0.5-meter). For example, there is a chance that the input to a deep model contains only the middle of the roof of a large building, which cannot provide the model with enough information for a successful decision. Although the exact reason for the failure cannot be identified, an error in a large building is common in deep learning-based methods (Ji et al., 2018). On the other hand, our method produced reliable, accurate building maps regardless of building size and shape.

Not only for huge and unique-shape buildings but also for residential areas where small buildings dominate the tile, our method outperformed Microsoft’s method as shown in the fifth row of Figure 6. Our algorithm extracts auxiliary units of houses such as garden sheds or detached garages well while many auxiliary units were not detected in Microsoft building footprints. This failure might be due to the limited resolution of the optical image used for generating building footprints or due to dense trees over residential buildings. Also, it could be due to the lack of training data for the auxiliary units. However, our algorithm was able to detect auxiliary units that are generally not detected by Microsoft’s algorithm (Heris et al., 2020). More discussion about the auxiliary unit is provided in Section 3.3 and Section 4.2.1.

## 3.2 Results of New York City dataset

Similar to Section 3.1., the three building maps (i.e., LiDAR building map, Microsoft Building Footprints, ground-truth) were compared using the tiling comparison method. New York City dataset also has a time discrepancy among different building maps. The authoritative building map of New York City is updated on a weekly basis by the DoITT team<sup>2</sup>.

<sup>2</sup><https://data.cityofnewyork.us/Housing-Development/Building-Footprints/nqwf-w8eh>

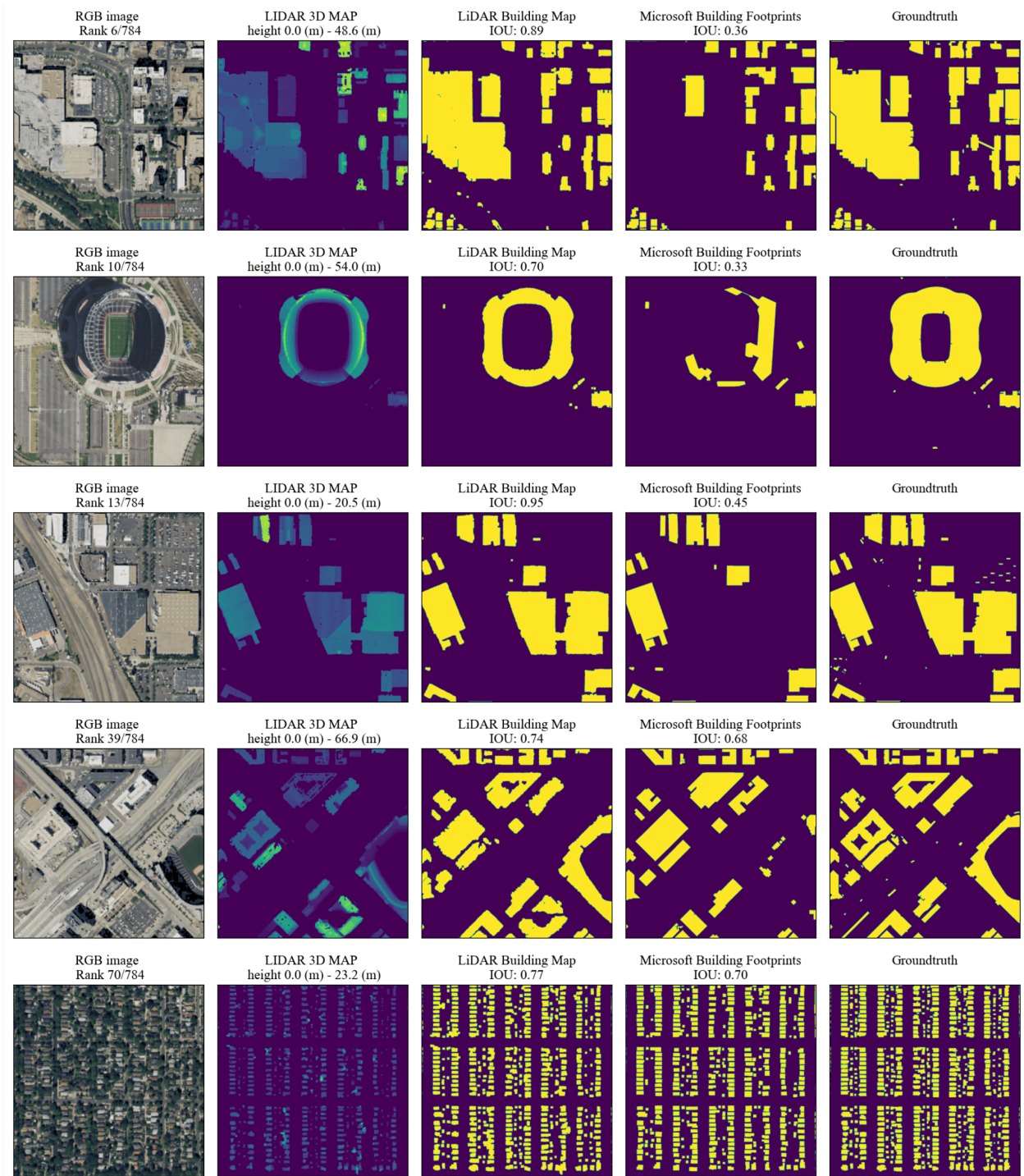


Figure 6: Five selected tiles and their building mapping results from the Denver dataset

The vintage of the authoritative building map for this experiment is February 2022. For Microsoft Building Footprints, less than 5% of total building labels had a time tag but most of them were 2019. LiDAR building map was generated with LiDAR data for 2014. The default parameter values, described in Section 2.2.3., were used for the entire area to produce the LiDAR building map.

### 3.2.1 Conventional quantitative results

LiDAR building map and Microsoft Building Footprints of the entire study area (357 km<sup>2</sup>) of the New York City dataset were evaluated in terms of IoU, precision, recall, and F1-score (Table 2). As a result, LiDAR building map obtained higher accuracy than Microsoft Building Footprints in all metrics except for the precision (The low precision is mainly related to the dilation kernel K3. A more detailed explanation is given in Section 4.2.3.). The result shows that our algorithm could outperform Microsoft’s algorithm overall, even with a larger time gap to the ground-truth. Considering that our algorithm used only a single parameter set for the entire area, the results show that our algorithm is scalable and robust.

Table 2: Conventional quantitative results of the New York City dataset

	IoU	Precision	Recall	F1-score
LiDAR building map	<b>75.9</b>	80.3	<b>93.2</b>	<b>86.3</b>
Microsoft Building Footprints	72.8	<b>84.6</b>	83.9	84.3

### 3.2.2 Tiling evaluation

Among 1428 tiles of New York City, we manually excerpted 5 tiles that rank high (top 10%) and show notable differences in building maps. Figure 7 shows RGB images and their corresponding 3D building map, LiDAR building map, Microsoft Building Footprints, and ground-truth. The RGB imagery is from NAIP’s orthoimagery. The RGB image was taken from 2015. Thus, we can expect the same buildings existing in both RGB image and ground-truth should exist in both LiDAR building map and Microsoft Building Footprints as both vintages of LiDAR building map (2014) and Microsoft Building Footprints (2019) are between those of RGB image (2015) and ground-truth (2022). Also, in the same way as Section 3.1.2., the ranking denoted with RGB image indicates the ranking of the largest difference between LiDAR building map and Microsoft building footprints. 3D building map generated by our method are also displayed for reference with its height range. IoU values calculated by comparing LiDAR building maps and Microsoft Building Footprints respectively to ground-truth are also provided.

Unlike the Denver dataset, most of the errors in the top ranks were from the sea. Although the net areas of errors were not relatively large, Microsoft Building Footprints often had some artifacts in water bodies as shown in the first row of Figure 7. A similar error was also observed from (Heris et al., 2020). Microsoft’s algorithm might have had trouble differentiating between buildings and other objects such as clouds, shadows, or ships over the sea. LiDAR building map generated by our method rarely had errors in water bodies as water bodies were pre-detected by the DTM generation method (Song & Jung, 2022) and were masked out. However, our algorithm also detected some large ships as buildings as shown in the third row of Figure 7. Although not displayed in Figure 7, errors in the LiDAR building map include small, disconnected terrains near coastlines. This is due to the limitation of the DTM generation method that can occur error terrain near the boundary of LiDAR data extent. More discussion of DTM-related errors is provided in Section 4.3.3.

On land, similar to the results of the Denver dataset, most of the errors in Microsoft Building Footprints were large buildings and uniquely shaped buildings. One example is an airport as shown in the second row of Figure 7. This is probably due to the lack of training samples for airports in the training dataset of Microsoft’s algorithm for the same reason that many errors occurred in the large, uniquely shaped buildings in the Denver dataset. One unique error in the LiDAR building map is that it sometimes considers airplanes as a building class. This is an obvious limitation of our method. Since our algorithm extracts building candidates by simply masking with a certain height and filters out sparse points and non-planar objects, large airplanes can be misclassified as buildings. Although not excerpted here, large trailers and cargos were other examples of misclassification in the LiDAR building map. Section 4.4.1. summarizes the potential error sources of our algorithm.

Another common error source was the time discrepancies among datasets. In the fourth row of Figure 7, the commission errors of the LiDAR building map are due to the time gap. The tile is from Rikers Island, New York. We found that some detected buildings (i.e., George Motchan Detention Center) in the LiDAR building map were demolished after the LiDAR data collection. Microsoft’s algorithm, however, failed to detect those buildings, which must have existed at the



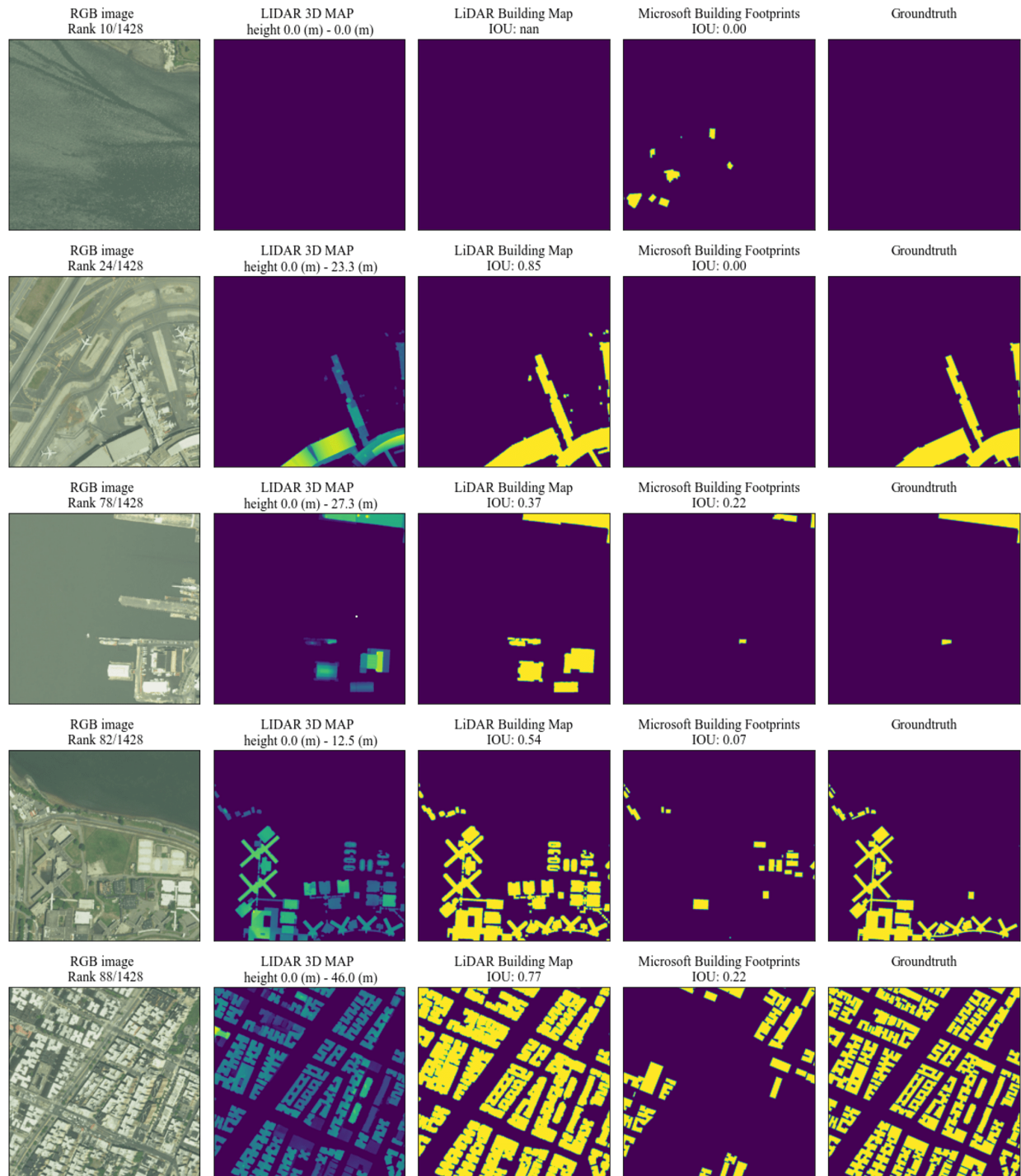


Figure 7: Five selected tiles and their building mapping results in the New York City dataset

time of the mapping. This failure might be either due to the uncommon shape of the buildings or the non-availability of cloud-free optical imagery. The fifth row of Figure 7 shows a significant difference between the building maps in the downtown area. The error in Microsoft’s algorithm seems neither due to the time gap nor the shape of the buildings. It might be due to the defect in an optical image used for the mapping. Compared to this unexpected, inexplicable error from the image-based Microsoft’s algorithm, errors in LiDAR building map are generally easier to be explained and our algorithm rarely has an error caused by the data itself. This is because our algorithm simply considers the physical property of the building, and LiDAR uses an active sensor and is not affected by clouds or other atmospheric conditions. Therefore, we can expect an explainable, complete, and accurate building map with our algorithm. It is a significant advantage of LiDAR-based building mapping over optical image-based building mapping. As errors from our algorithm are generally more explainable and predictable than image-based building mappings, uncertainties of the building map could be significantly relieved and errors could be more controllable, which could be beneficial to subsequent analyses that use building maps. Furthermore, even though acquiring optical images could be cheaper than performing ALS, having cloud-free high-resolution images over a large area would be very expensive and may be even impossible for timely applications, such as disaster management and humanitarian aid. One drawback of our algorithm is that it can produce “fat” buildings, as shown in the fifth row of Figure 7. This is related to the dilation with the parameter K3, and this is the main reason why the precision of the LiDAR building map is lower than that of Microsoft Building Footprints in Table 2. More discussion about K3 and its impact is provided in Section 4.2.3.

### 3.3 Error analysis

#### 3.3.1 Omission error

We observed both our algorithm and Microsoft’s algorithm often fail to detect small buildings. To evaluate the performance, focusing on small-to-medium sized buildings ( $<1,000 \text{ m}^2$ ), of the LiDAR building map and Microsoft Building Footprints, we counted the number of correctly detected buildings for different building areas. The building area refers to the area of each building’s footprint. We defined a “correctly detected building” as an instance that exists in the ground-truth and its overlapped portion with generated building instances is more than 50%. Figure 8 and Figure 9 show the number of correctly detected buildings according to the building area for the Denver dataset and New York City dataset, respectively. The “Number of Buildings” in those graphs refers to the number of buildings in ground-truth for each building area category. It shows the distribution of the number of buildings in the ground-truth according to the building area and the performance trend of the two algorithms. Quantitative results of algorithms by building area are detailed in later paragraphs. Only buildings smaller than  $1,000 \text{ m}^2$  were illustrated as the performance significantly varied in relatively small buildings ( $<100 \text{ m}^2$ ) and the trend was generally maintained for larger buildings.

For the Denver dataset, both our algorithm and Microsoft’s algorithm struggled to detect buildings smaller than  $50 \text{ m}^2$ . Most of the buildings smaller than  $50 \text{ m}^2$  are accessory units such as storage sheds or detached garages. In the New York City dataset, the ratio of correctly detected buildings was significantly larger than that of the Denver dataset. This is because the authoritative building map of the New York City dataset did not label storage sheds as a building class, while that of the Denver dataset labeled storage sheds as a building class. Since our algorithms used an erosion filter with a kernel size (K1) of 7 by 7 based on the assumption that buildings are larger than 3.5-meter by 3.5-meter squares, some of the buildings smaller than around  $10 \text{ m}^2$  (most of the storage sheds) were removed. By changing to the smaller K1 value, buildings smaller than  $10 \text{ m}^2$  can be detected better, but the chance of detecting dense trees as a building class might increase. More discussion about this trade-off is discussed in Section 4.2.1.

It should be noted that the significantly different statistics between the two study areas indicate that even authoritative maps are not consistent as building definitions may vary for different states and countries. Considering this issue, our algorithm may have the advantage to provide more consistent results based on the clear rule determined by an algorithm.

Figure 10 provides the number of buildings in the ground-truth of the Denver and the New York City datasets. Each category is intended to represent the different types of buildings. The categorization of building in this paper consists of four classes with different ranges of area:  $0\text{-}50 \text{ m}^2$  (“accessorial class”),  $50\text{-}500 \text{ m}^2$  (“residential class”),  $500\text{-}10,000 \text{ m}^2$  (“commercial class”), and  $10,000 \text{ m}^2\text{-}$  (“mega-size class”).

The first category represents accessorial buildings. The accessorial class can include storage sheds, detached garages, containers, tents, treehouses, portable cabins, and lighthouses. Some building types in this category are often excluded from a building class in some classification systems. Specifically, the authoritative map of the Denver dataset categorized storage sheds into its building class while that of the New York City dataset excluded storage sheds from its building class. The second category, the residential class, represents most of the residential buildings with typical size. This category accounts for the majority of buildings. The third category, the commercial class, represents large commercial buildings. This category may include office buildings, retails, hospitals, warehouses, and industrial buildings. The last category represents mega-size buildings such as large shopping malls, factories, train stations, airports, and sports

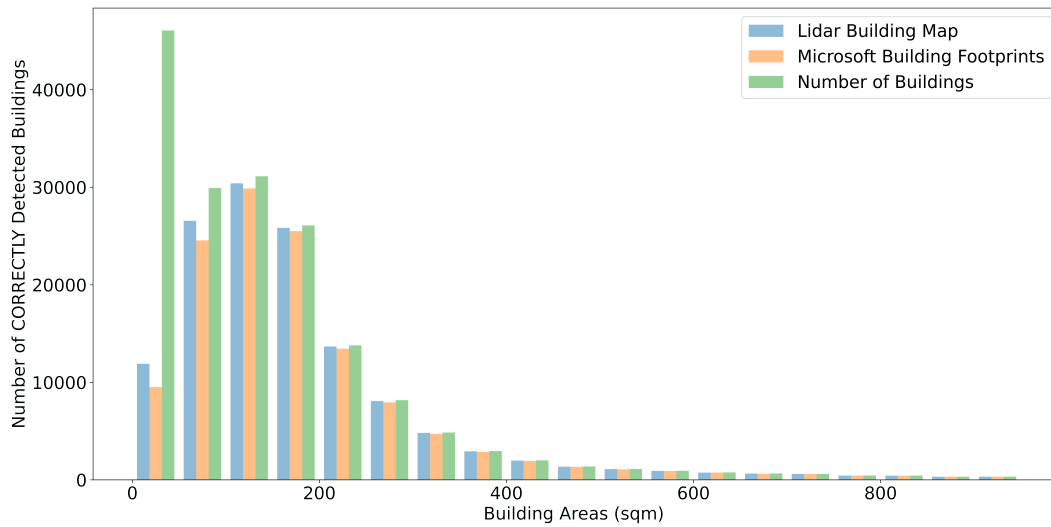


Figure 8: The numbers of correctly detected buildings and the number of buildings in the ground-truth according to the building area (0-1,000 m<sup>2</sup>) in the Denver dataset

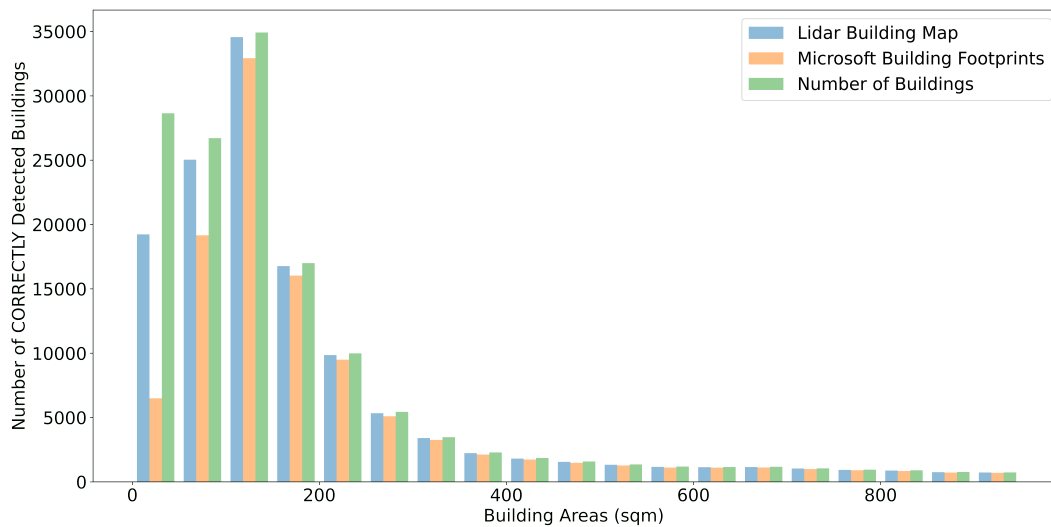


Figure 9: The numbers of correctly detected buildings and the number of buildings in the ground-truth according to the building area (0-1,000 m<sup>2</sup>) in the New York City dataset

	Accessorial Building (0-50 sqm)	Residential Building (50-500 sqm)	Commercial Building (500-10,000 sqm)	Mega-size Building (10,000 sqm-)
Denver dataset	46071	120271	10335	170
New York City dataset	28647	103259	23621	435

Figure 10: The number of buildings in ground-truths according to the building area (Icon copyright: Flaticon)

complexes. Based on this categorization, we counted the number of correctly detected buildings in both datasets (Denver and New York) and compared the detection performance of our method with that of Microsoft’s algorithm. Although the type of building cannot be classified by only their areas, this categorization can provide a sense of the performance of algorithms according to the building types.

Table 3 and Table 4 show the detection (true positive) rate of each category respectively for the Denver and New York City datasets. The detection rate refers to the ratio of the number of correctly detected buildings to the number of buildings in ground-truth for each category.

Table 3: Detection (true positive) rates according to the building area in the Denver dataset

	0-50 (m <sup>2</sup> )	50-500 (m <sup>2</sup> )	500-10,000 (m <sup>2</sup> )	10,000- (m <sup>2</sup> )
LiDAR building map	<b>25.8</b>	<b>96.1</b>	<b>98.4</b>	<b>97.6</b>
Microsoft Building Footprints	20.6	93.3	97.1	92.4

Table 4: Detection (true positive) rates according to the building area in the New York City dataset

	0-50 (m <sup>2</sup> )	50-500 (m <sup>2</sup> )	500-10,000 (m <sup>2</sup> )	10,000- (m <sup>2</sup> )
LiDAR building map	<b>67.1</b>	<b>97.4</b>	<b>97.7</b>	<b>96.1</b>
Microsoft Building Footprints	22.7	88.4	94.2	89.0

In the Denver dataset, both methods performed poorly in the accessorial building class. However, in the New York City dataset, the performance gap between ours and Microsoft’s algorithm was significant. Our method produced a 67.1% detection rate while Microsoft’s algorithm produced a 22.7% detection rate in the accessorial building class. The significant difference between the Denver and New York City datasets is due to the difference in their classification system. Storage sheds, which account for a large portion of building counts, were classified as building in the authoritative map of the Denver dataset, while that of the New York City dataset does not include storage sheds as a building class. Since most of the storage sheds, which account for the majority of the accessorial building class in Denver, were not detected well in both methods, the detection rates for accessorial buildings were poor in both methods. On the other hand, in the New York City dataset, as storage sheds (which are difficult to be detected by both algorithms) were not included in the building class, the performance gap between the two methods becomes evident.

Although the detection accuracy per exact building type was not identified in our experiment, we found there was a noteworthy difference between the distributions of the two datasets. 52.0% of buildings from the accessorial building class were less than 20 m<sup>2</sup> in the Denver dataset, while only 17.9% of accessorial buildings were less than 20 m<sup>2</sup> in the New York City dataset. Considering that most of the storage sheds are smaller than 20 m<sup>2</sup>, we can conclude the difference in their classification systems made the performance gap in accessorial building class of the New York City dataset more evident.

Except for the accessorial category, our algorithm produced a detection rate of over 95.0% in all cases. Microsoft’s algorithm also produced a good performance in general, but our method outperformed Microsoft’s algorithm in detection rate for all cases.

### 3.3.2 Commission error

Commission error accounts for a relatively small portion of the total error in both algorithms. The time discrepancy to ground-truth accounts for some portions of the reason for the commission error. Except for this, most of the commission errors of our algorithm were dense trees or DTM-related artifacts. These error sources are the limitation of our method. Detailed analyses of these limitations are described in Section 4.3.

Similar to the omission error, we tabulated commission (false positive error) rates of the LiDAR building map and Microsoft Building Footprints according to the building area. Table 5 and Table 6 show the commission rates respectively for the Denver and New York City datasets. The commission rate refers to the number of incorrectly detected buildings out of the total number of buildings in ground-truth. The "incorrectly detected building" is defined as an instance that exists in generated building map (i.e., LiDAR building map or Microsoft Building Footprints) but its overlapped portion with the ground-truth is less than 50%. As a result, LiDAR building maps produced higher commission errors than Microsoft Building Footprints. Particularly, the commission rate for the accessorial building class in the New York City dataset is larger than others. This is closely associated with the fact that the LiDAR building map showed a high detection rate in the accessorial building class of the New York City dataset. Simply put, as our method detected accessorial buildings much more than Microsoft’s algorithm, the LiDAR building map has more positives (either true or false) than Microsoft Building Footprints in the accessorial building class.

The poor performance in the accessorial category is partly due to the definition of the correctly detected building in our study. We defined the correctly detected building as an instance that exists in ground-truth and its overlapped portion with generated building instances is more than 50%. Generally, since errors in building footprints tend to occur near the building boundary, the definition of the correctly detected building leads to a harsher standard for small buildings as the proportion of the building boundary is necessarily larger for small buildings than for large buildings.

Table 5: Commission (false positive) rates according to the building area in the Denver dataset

	0-50 (m <sup>2</sup> )	50-500 (m <sup>2</sup> )	500-10,000 (m <sup>2</sup> )	10,000- (m <sup>2</sup> )
LiDAR building map	4.3	2.6	2.8	1.2
Microsoft Building Footprints	<b>2.4</b>	<b>0.6</b>	<b>0.8</b>	<b>0.6</b>

Table 6: Commission (false positive) rates according to the building area in the New York City dataset

	0-50 (m <sup>2</sup> )	50-500 (m <sup>2</sup> )	500-10,000 (m <sup>2</sup> )	10,000- (m <sup>2</sup> )
LiDAR building map	19.1	4.6	2.5	6.0
Microsoft Building Footprints	<b>6.5</b>	<b>1.5</b>	<b>1.3</b>	<b>1.8</b>

## 3.4 Summary of results

Section 3 provided experimental results of our algorithm compared to Microsoft’s algorithm. Quantitative and qualitative analyses with extensive experimental areas showed that our algorithm outperformed Microsoft’s algorithm in the majority of criteria. To be specific, our algorithm produced higher IoU, recall, and F1-score in both Denver and New York City datasets. Our algorithm’s detection rates were higher than that of Microsoft’s algorithm in all categories of building. Also, we found that our algorithm was generally better at detecting large and uniquely shaped buildings than Microsoft’s algorithm. However, our algorithm produced lower precision in the New York City dataset and had higher commission rates in all building categories than Microsoft’s algorithm.

Our algorithm is an unsupervised method. It does not need any training samples and does not require any prior knowledge of the experimental area. Also, our algorithm used only a single set of parameters for an entire 550 km<sup>2</sup> area but produced better results in general than Microsoft’s algorithm which used millions of building labels and required post-processing for trimming building boundaries. Moreover, errors in our algorithm are easy to be explained while errors in Microsoft’s algorithm are often hard to be clearly explained. These results indicate that, given the decent quality of airborne LiDAR data, our algorithm can be a good alternative to image and deep learning-based algorithms for 2D and 3D building mappings.

## 4 Discussion

### 4.1 Overview of discussion

The results in Section 3 demonstrated the great potential of our building mapping method that leverages the physical properties of building (i.e. ground-standing, laser-impermeable, and relatively smooth) in airborne LiDAR data with an unsupervised method. Nevertheless, we observed some limitations and errors in our building maps. With more exhaustive experiments, we found some errors could be prevented with parameter tunings, but some limitations are difficult to avoid.

Our discussion in this section elaborates on the limitations and possible remedies for those limitations. To explore our algorithm’s limitations more in-depth, we added other study areas outside of the Denver and New York City datasets to add more diversity. The additional study areas include other large cities, small towns in tropical regions and mountainous areas, uninhabited natural areas, and so forth. First, in Section 4.2., we discussed some influential parameters in our algorithm and showed how they affect the results and how they can be adjusted to reduce errors. Second, in Section 4.3., we described some limitations that were not easily resolved even with the parameter tuning. Lastly, in Section 4.4., we discussed the scalability of our algorithm for global-scale mapping.

### 4.2 Suggestion for parameter tuning

Although the proposed algorithm with the default parameter can outperform Microsoft’s algorithm in general, we have found that proper parameter tuning can improve its performance even more in some cases. Examples include the case when one has a certain preference for accessorial buildings (related to parameter K1) and the case when one tries to map an area with lots of dense trees (related to parameter DT). Also, we found adjusting building boundaries (related to parameter K3) can significantly affect the quantitative metrics. In this subsection, we discuss influential parameters and provide general tips for parameter tuning.

#### 4.2.1 K1 parameter tuning for handling accessorial buildings

Our algorithm involves erosion and dilation with a pre-determined kernel size (K1). Generally, as K1 gets larger, commission error decreases while omission error increases. This is because both small buildings and dense trees are more likely to be removed during erosion with a larger K1 value. To be specific, small buildings whose width is shorter than K1 will be removed by the erosion kernel. As typical residential houses are larger than 3.5-meter by 3.5-meter, default K1= 7 for the 0.5-meter resolution case will not remove usual residential buildings. However, some accessorial or small buildings like detached garages, garden sheds, and trailers can be removed with the default K1 value. As for the tree case, the erosion kernel removes most of the trees. This is because the LiDAR penetrates the trees and observes the ground beneath the tree, and eventually makes trees like salt-and-pepper noise-like small patches. However, some dense trees that do not allow penetration and are represented as a contiguous group of patches with a size larger than K1 by K1 pixels will still remain after the erosion kernel. This is why the planarity-based filtering with the parameter DT is needed.

Figure 11 shows five sample areas from the Denver dataset that showed notable differences for different K1 values. In Figure 11, "Building correct" refers to the pixel which both LiDAR building map and ground-truth classified as building. "Non-building correct" refers to the pixel which both LiDAR building map and ground-truth classified as non-building. "Errors" indicates the pixel where LiDAR building map resulted in different results to the ground-truth. The default value for K1 used for the experiment in Section 3 was 7. The first row of Figure 11 shows an example of a commission error that can occur when K1 is too small. Containers were not labeled as building in the Denver ground-truth data, but K1 of 5 detected some containers as buildings. This is because some containers’ widths are larger than 2.5-meter. On the other hand, K1 of either 7 or 9 did not classify containers as buildings. The second and third rows of Figure 11 show the example where K1 of 9 was not able to detect detached garages as buildings while both smaller K1s detected them as buildings. The fourth row and fifth rows of Figure 11 show the example of storage sheds. The smaller the value of K1, the more often the storage shed was classified as a building. The fifth row shows the example of overhanging dense trees as well. With the smaller K1, overhanging dense trees are more likely to be detected as buildings.

We also quantitatively evaluated the impact of K1 by mapping the Denver dataset with different K1 values. Table 7 and Table 8 show the detection rate and the commission rate, respectively. The accessorial building class (0-50 m<sup>2</sup>) showed a significant difference in the performance for different K1 values. With the smaller K1, the detection rate increased but the commission rate increased as well. In other words, the smaller K1 is more likely to map small, accessorial buildings, but at the same time, it is more likely to classify dense trees as buildings. In contrast, the larger K1 could prevent the commission error but may miss some small buildings.

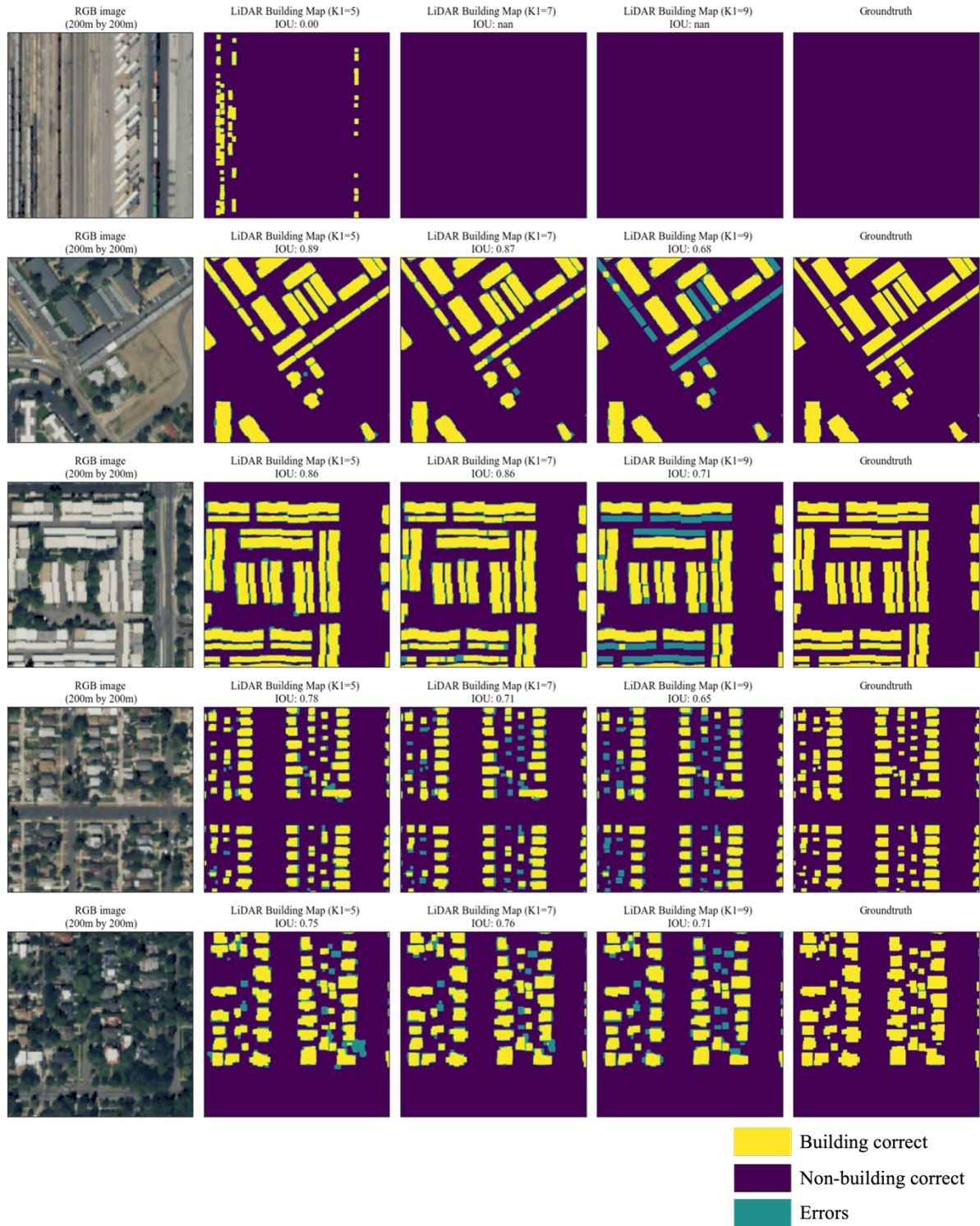


Figure 11: LiDAR building maps with different K1 values

Table 7: The impact of parameter K1 on the detection (true positive) rates in the Denver dataset

	0-50 (m <sup>2</sup> )	50-500 (m <sup>2</sup> )	500-10,000 (m <sup>2</sup> )	10,000- (m <sup>2</sup> )
LiDAR building map (K1=5)	<b>40.5</b>	<b>97.4</b>	<b>98.5</b>	<b>97.6</b>
LiDAR building map (K1=7, default)	25.8	96.1	98.4	<b>97.6</b>
LiDAR building map (K1=9)	13.2	91.5	98.1	<b>97.6</b>

Table 8: The impact of parameter K1 on the commission (false positive) rates in the Denver dataset

	0-50 (m <sup>2</sup> )	50-500 (m <sup>2</sup> )	500-10,000 (m <sup>2</sup> )	10,000- (m <sup>2</sup> )
LiDAR building map (K1=5)	12.9	3.5	3.2	<b>1.2</b>
LiDAR building map (K1=7, default)	4.3	2.6	2.8	<b>1.2</b>
LiDAR building map (K1=9)	<b>1.9</b>	<b>2.0</b>	<b>2.6</b>	<b>1.2</b>

As shown above, our method can adjust the resulting building map to fit to the classification scheme by tuning K1. Therefore, unlike deep learning approaches, which may require re-labeling of training data to fit into different classification schemes, our method has an advantage in that it is unsupervised but adaptable to different classification schemes by simply tuning parameters according to purpose. Moreover, the results suggest that the building map produced from our method could be a good alternative to the authoritative building map as well in terms of consistency and scalability. This is because the criteria of a building can be different in authoritative maps as we observed the difference in the classification scheme between the Denver and the New York City datasets. On the contrary, our method would provide more consistent results than other maps, particularly if the building area is the main consideration of the classification system.

#### 4.2.2 Dense trees (DT) parameter tuning for forested areas

The parameter DT also affects the trade-off between omission and commission errors. Our algorithm has the planarity-based filtering with the parameter DT as some dense trees can still remain after the morphological filtering. As the value of DT increases, dense trees are likely to be removed, but buildings under overhanging trees are also likely to be removed.

Since the Denver and New York City datasets do not have many dense trees, we excerpted the case of a town in Callaway, Florida, US. This study area is around 11 km<sup>2</sup> and includes residential areas and tropical evergreen trees with densely multi-layered leaves. The laser scanning was conducted with a Riegl Q-1560 LiDAR system, and the point density was approximately 7-points/m<sup>2</sup>. As the ALS was conducted from April to May of 2017, we can expect a fully leaf-on condition. Figure 12 shows the satellite image and building map generated by our method with the default parameter set.

To explore the impact of DT values, we calculated quantitative metrics from this study area with different DT values. IoU, precision, recall, and F1-score with different DT values are plotted in Figure 13. For the calculation, we regarded Microsoft Building Footprints as the ground-truth as a more reliable ground-truth was not available over the Callaway area. The results turned out that the optimal value for DT in this study area was 0.35 and produced 0.68 IoU, while the default value of DT (0.1) produced 0.66 IoU. This indicates that proper selection of DT can increment accuracy slightly, but the default value still can produce reasonable accuracy. Also, the plateau in the graph of IoU between DT values of 0.05-0.5 was observed. It suggests that the default DT value would produce near-optimal results in general cases and that the performance is not sensitive to DT as long as DT is in the proper range.

Although DT of 0.35 produced the highest IoU value, it does not necessarily guarantee the best building map. Figure 14 shows the subset of the study area in Callaway, Florida, US. The figure illustrates the generated maps with planarity values according to different DT values. The planarity map shows the generated building map for different DT values, together with the planarity value of each building (The calculation of planarity is described in Section 2.2.3). As described in Section 2.2.3., DT value functions as a threshold to filter-out non-building objects among building candidates considering the planarity of the object. The figure with DT= 0 shows all building candidates before the planarity-based filtering because no building is filtered-out as DT was 0. With the default value (DT= 0.1), most dense trees were removed, but some non-building objects still remained. When DT was 0.2, only building objects were extracted. However, when DT was 0.3, two building objects with lower planarity values were removed. We found that two removed objects were actual buildings under overhanging trees through Google Street View. Therefore, for



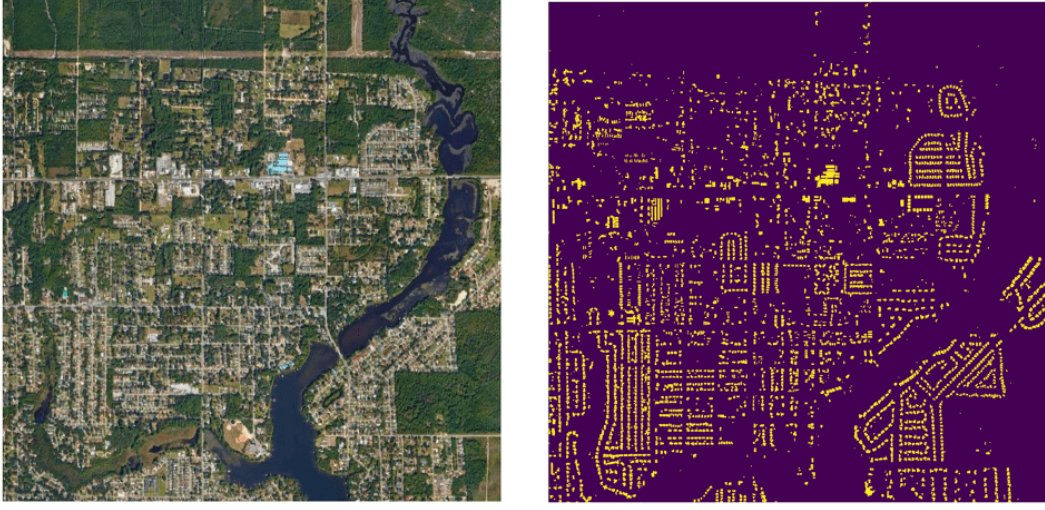


Figure 12: Satellite image and LiDAR building map of the Callaway dataset (3.3-km by 3.3-km)

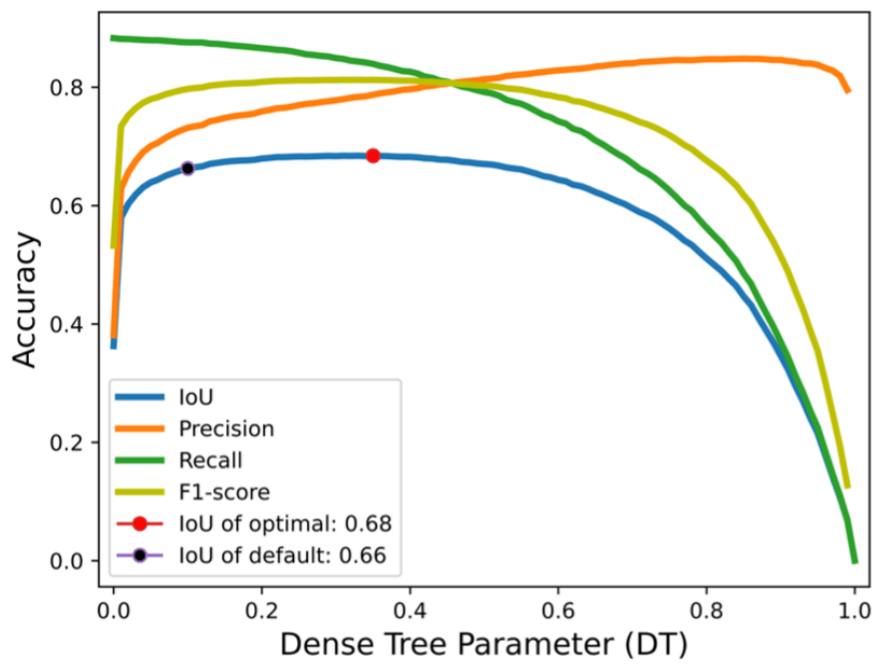


Figure 13: IoU, precision, recall, and F1-score according to the parameter DT in the Callaway dataset

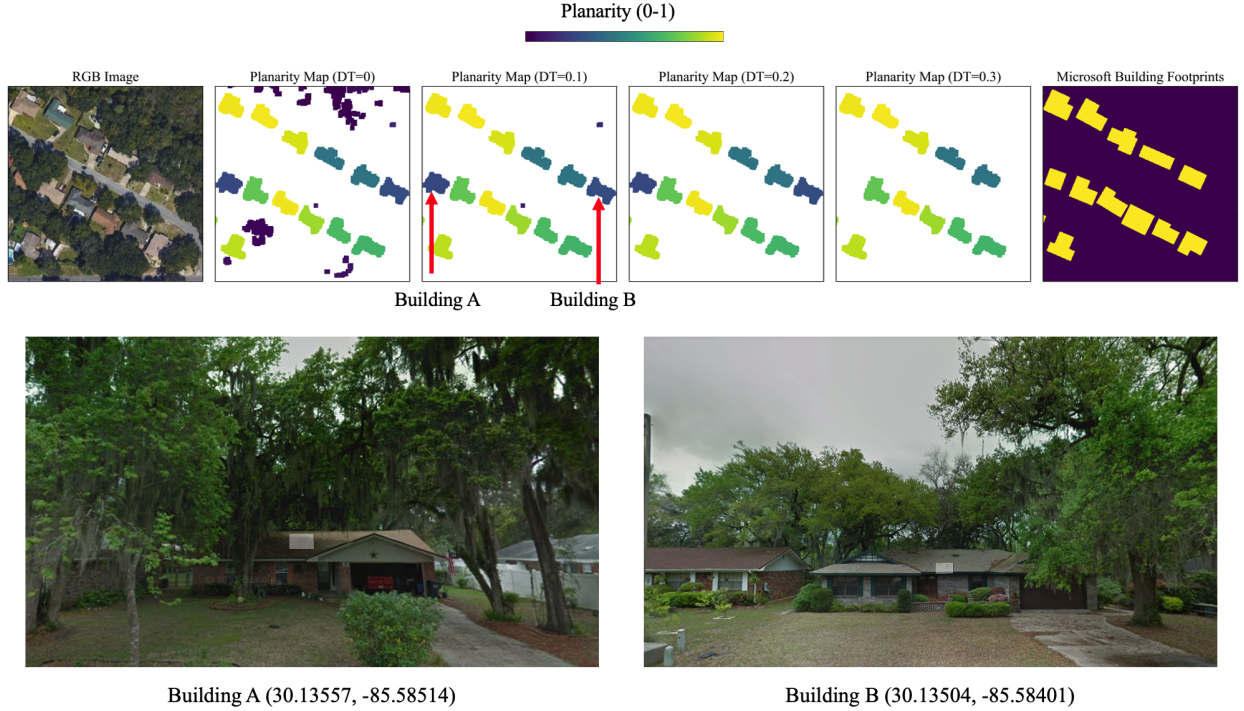


Figure 14: Examples of building maps (planarity maps) in the Callaway dataset according to the parameter DT and examples of buildings under overhanging trees in Google Street View (Image copyright: Google Inc.). The numbers in parentheses indicate the latitude and longitude of the building in decimal degrees, respectively.

this particular scene, the best DT was 0.2. The results suggest that the best DT value can be different according to the study area. Moreover, especially in the tropical regions, we observed several cases where a building under overhanging trees has a lower planarity value than the dense trees. This kind of reversal case can happen more when the LiDAR point density is lower, and it remains as a limitation of our algorithm. A more in-depth discussion on the impact of the LiDAR point density is provided in Section 4.3.2.

We also performed our algorithm on some uninhabited dense forests to investigate how many dense trees are classified as a building class. Study areas and LiDAR data collection dates are listed as follows: Monongahela National Forest (9 km<sup>2</sup>, November – December of 2016), West Virginia, US, Yellowstone National Park (4.5 km<sup>2</sup>, September–October of 2020), Wyoming, US, and Apalachicola National Forest (9 km<sup>2</sup>, March–May of 2018), Florida, US. Since these areas are development restricted areas, we can assume there is no building. As a result of the default parameter, the Monongahela National Forest dataset results in 8 false building objects, the Yellowstone National Park dataset results in 31 false building objects, and the Apalachicola National Forest dataset results in 11 false building objects. The total area of false building objects was less than 0.5% of entire areas in all cases. Although not all extracted objects were identified, most of them were trees or huge rocks. Also, 68% of them were less than 50 m<sup>2</sup>, which belongs to the category of the accessory building class. The results indicate that our algorithm even with the default parameter rarely produces false-positive errors in densely forested areas. However, if the experimental area includes a very large forested area, parameter tuning (e.g., using larger K1 and DT) is recommended to suit the purpose of the experiment.

#### 4.2.3 Dilation kernel (K3) parameter tuning for adjusting building boundaries

The dilation kernel size (K3) is for recovering underestimated building size. LiDAR observations near building boundaries are the mixed observations of ground points and building edges. This is because a typical airborne LiDAR scanner collects data points by emitting laser pulse radially with a whiskbroom pattern. Since the scan angle is not always perpendicular to the object on the ground, both the side and floor height values of the building can be collected as the height values of the building boundary.

Figure 15 shows a toy example of an ALS. The blue pixel will have multiple points with mixed elevations of the bottom, side, and top of the building. Among these mixed elevations, we used the bottom elevation for its DSM value to make a differentiation between building and tree easier as described in Section 2.2.1. Taking the lowest elevation

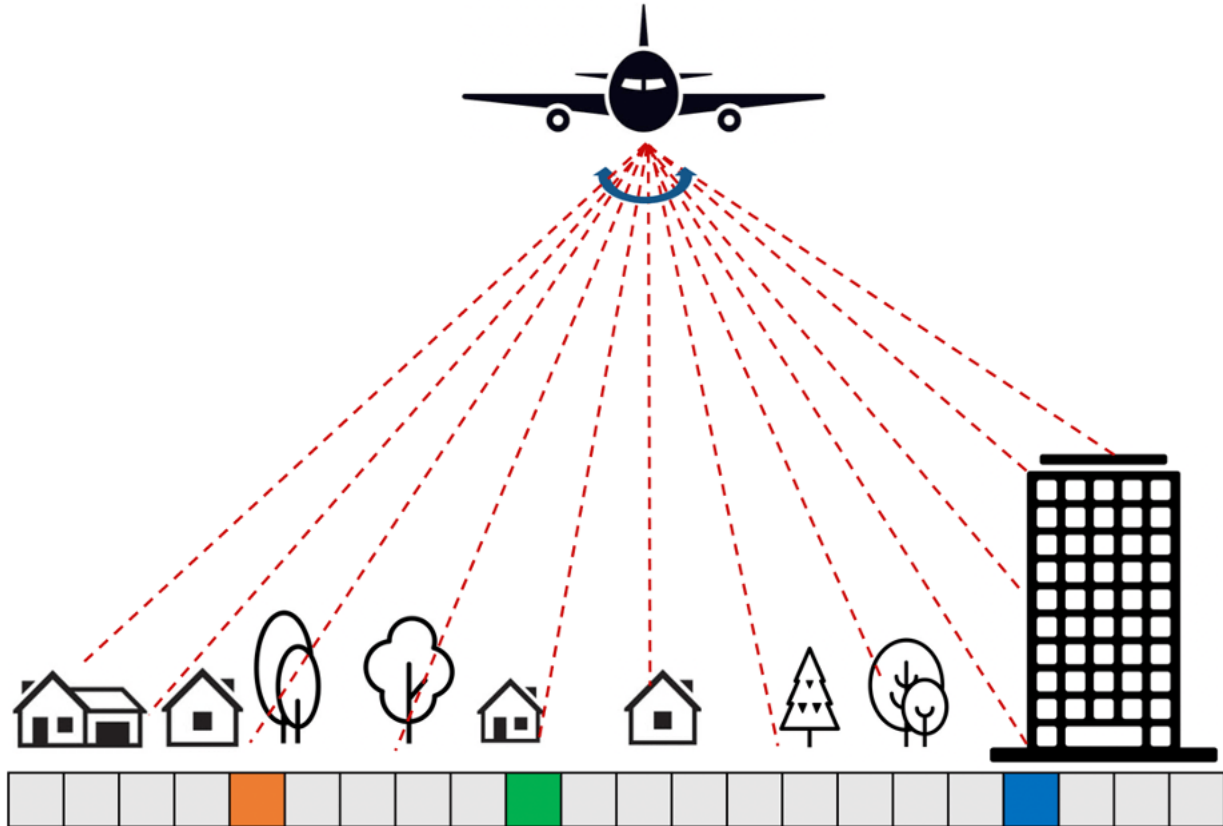


Figure 15: Graphical representation of airborne laser scanning

for DSM creation is good for the differentiation between buildings and trees, but it can result in the underestimation of the building boundary areas. Also, even if multiple points are not acquired for one pixel, the building area can be underestimated. In the green pixel in Figure 15, for example, since the laser measures the elevation of the bottom, the green pixel will be classified as a non-building pixel. The case of the orange pixel will have the same result, and it will cause the underestimation of the building boundary. Of course, if LiDAR collects the point from the edge of the building roof, the building area can be overestimated up to the one-pixel resolution. However, creating DSM by taking the lowest elevation among multiple points in the same grid is more likely to underestimate the building area overall. Also, the morphological filtering with K1 tends to make buildings smaller (please refer to Figure 20). In fact, the thickness of the underestimated boundary is affected by several variables, including the point density, the scan angle, and the relative position between the laser beam firing point and each individual object. Ideally, the kernel size (K3) must be tuned for each pixel considering those variables. However, some required variables are not provided in most laser scanning data, and calculating optimized K3 for every pixel will significantly increase the computation.

Based on the quantitative evaluation, we confirmed the default value 5 for K3 produced reasonable accuracy in general. However, we also found that the K3 value significantly affects the accuracy of building mapping and the optimal value may vary depending on experimental areas. Table 9 and Table 10 show the quantitative results for different K3 values from the Denver and New York City datasets, respectively. K3 of 5 showed the highest IoU performance in the Denver dataset while K3 of 3 showed the highest IoU performance in the New York City dataset. Figure 16 provides examples of boundary errors with different K3 values in the Denver dataset. "Building correct" refers to the pixel which both LiDAR building map and ground-truth classified as building. "Non-building correct" refers to the pixel which both LiDAR building map and ground-truth classified as non-building. "Errors" indicates the pixel where LiDAR building map resulted in different results to the ground-truth.

The reason for the inconsistent optimal K3 value can be attributed to the following three reasons. First, as described early, the optimal K3 should be determined by the function of the scan angle and the relative position between the sensor and the object. However, these conditions are not uniform due to the nature of the ALS data acquisition mechanism, which makes it challenging to optimize K3 value globally. Second, the ground-truth itself has an inconsistency as well.

Since the ground-truth was labeled by different surveyors using optical images of different specifications, there is a chance that optical images were not in the same condition in terms of their resolutions and ortho-rectification qualities. Also, there could have been some human biases and errors during labeling. Lastly, the building orientation on the ground might contribute to the inconsistency. The building orientation issue is discussed in Section 4.3.4.

As the dilation with K3 is the last step of our algorithm, it is always possible to tune the kernel size to fit the target area after the initial mapping without the last dilation. Therefore, finding an optimal single K3 value would not be a difficult job. However, our method has a limitation in that it currently has a global K3 value and it cannot apply different sizes of dilation kernel for individual objects.

Table 9: The impact of parameter K3 on the quantitative metrics in the Denver dataset

	IoU	Precision	Recall	F1-score
LiDAR building map (K3=1)	70.1	<b>95.6</b>	72.4	82.4
LiDAR building map (K3=3)	77.6	94.2	81.4	87.4
LiDAR building map (K3=5, default)	<b>81.8</b>	91.2	88.8	<b>90.0</b>
LiDAR building map (K3=7)	80.5	85.6	<b>93.2</b>	89.2

Table 10: The impact of parameter K3 on the detection (true positive) rates in the New York City dataset

	IoU	Precision	Recall	F1-score
LiDAR building map (K3=1)	77.0	<b>89.4</b>	84.7	87.0
LiDAR building map (K3=3)	<b>77.9</b>	85.3	90.0	<b>87.6</b>
LiDAR building map (K3=5, default)	75.9	80.3	93.2	86.3
LiDAR building map (K3=7)	72.2	75.1	<b>94.8</b>	83.9

#### 4.2.4 Other parameter tunings

Other parameters that can be considered in our algorithm include the spatial resolution of the building map, water buffer, and height threshold. We adopted the 0.5-meter resolution for all experiments in this paper because the ground-truth or Microsoft Building Footprints were made mostly based on a typical high-resolution satellite image, which has around 0.5-meter resolution. Any finer resolutions are always possible with the fine rasterization method as long as high point density LiDAR data and computational resources are available. We used the water mask generated by the DTM generation algorithm Song & Jung (2022). Although the cases were very rare, we observed some trees near the water body can be extracted as buildings. This can happen when trees are surrounded by water pixels. During the interpolation of empty grids in DTM generation, empty grids caused by water are likely to be interpolated with the elevation values of nearby trees, so they can be classified into the building class. In most cases, putting a buffer of 5- to 10-meter to the water mask can remove those errors. For the Denver and New York City datasets, we used a 5-meter buffer. Lastly, if there is any preferred height range for building classification, choosing different HT values instead of the default HT of 1.5-meter would be beneficial.

### 4.3 Limitations of our method

Most of the limitations of our algorithm can be resolved to some extent by proper parameter tuning as discussed in Section 4.2. Also, most of the limitations are essentially associated with the trade-off between commission and omission errors. However, some limitations are not directly associated with the trade-off. This section devotes to discussing those limitations.

#### 4.3.1 Error near skyscrapers

As opposed to the optical image data, LiDAR is not affected by shadow. However, like optical images, it still can be affected by occlusion as LiDAR emits laser pulse having a slant scan angle as depicted in Figure 15. This property can result in cases where LiDAR points were not collected in-between closely clustered tall buildings. This case may happen particularly near skyscrapers. Laser scanning at a higher altitude and with a smaller scan angle will alleviate the



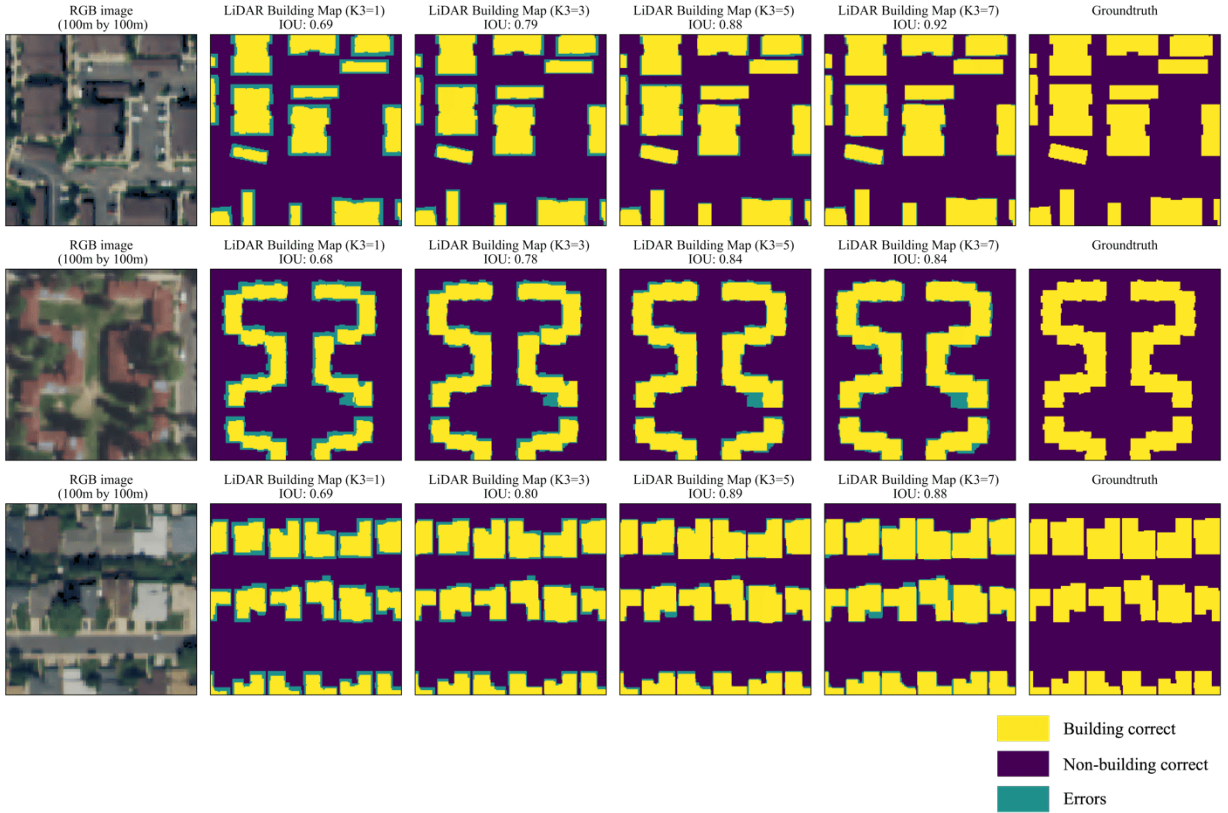


Figure 16: LiDAR building maps according to different K3 values

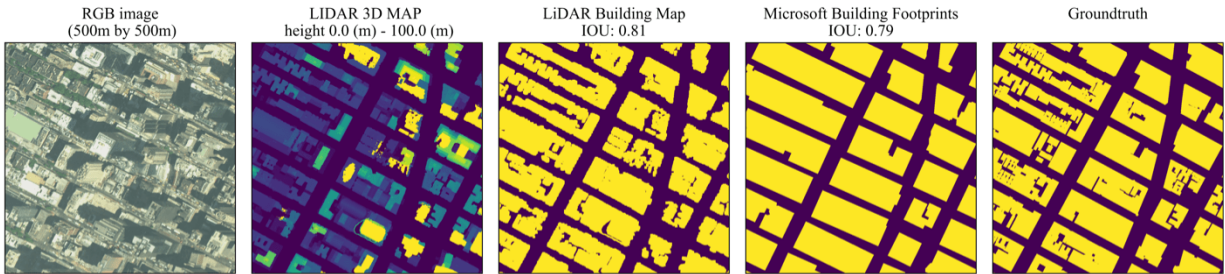


Figure 17: Errors by occlusion in skyscrapers

occlusion issue, but the cost of data collection would increase significantly. Figure 17 shows an example of Manhattan, New York. The occluded area due to skyscrapers resulted in either blurred boundaries or holes in the building map.

#### 4.3.2 Low point density scenarios

We have discussed that a dense tree can be a false positive error in Section 4.2.2. This error occurs particularly often when trees are close to the building. Note the orange pixel in Figure 15. Since the laser penetrates the tree, the orange pixel will be classified as a non-building class, and it allows the separation between the building and the tree. However, if the tree is too dense to allow the laser penetration, the building and the tree will be merged into one object of the building candidate. If merged, it could either be removed or remain based on its planarity, which eventually results in either omission or commission error, respectively. Naturally, this error can occur more frequently if point density is low.

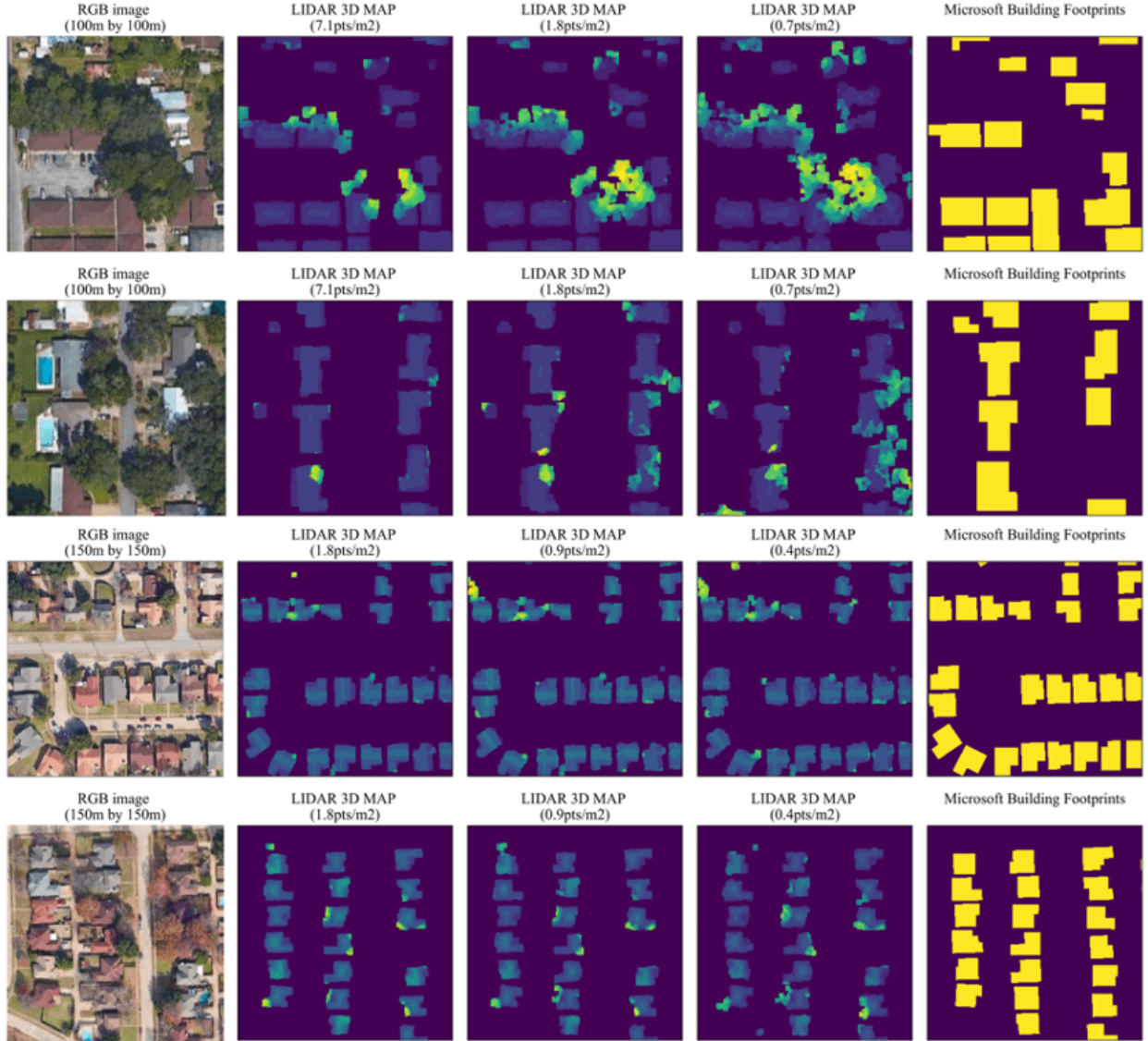


Figure 18: Errors by overhanging dense trees in low point density scenarios

To investigate the impact of the point density, we created low point density LiDAR data by subsampling the original LiDAR data. Figure 18 displays several of the most difficult examples with overhanging dense trees. The first two rows are excerpted from Callaway, Florida, US, and the last two rows are excerpted from Dallas, Texas, US. LiDAR data were scanned from April to May of 2017 for the Callaway dataset and from April to July of 2019 for the Dallas dataset, respectively, which guarantees the season of fully leaf-on trees. A Riegl Q-1560 LiDAR system and a Leica ALS80 were used for the Callaway dataset and the Dallas dataset, respectively. RGB satellite images were from Google Earth. To visualize the overhanging trees effectively, LiDAR 3D maps were provided together. Microsoft Building Footprints are also provided for reference.

As the point density decreases (Figure 18), some dense trees are classified as buildings, increasing the commission error. Also, it results in an unreliable 3D building map when dense overhanging trees are over the building. Nevertheless, even with the very low point density scenario ( $<1$ -points/m<sup>2</sup>), our algorithm was able to properly detect buildings if they have no overhanging trees. However, a low point density example will lose the detail of the building map. These results suggest that the performance of our algorithm will further be improved as point density increases.

### 4.3.3 Commission errors due to the DTM

The scalability of our building mapping algorithm can attribute its success partly to the DTM generation algorithm that we adopted Song & Jung (2022). As the DTM generation algorithm can extract water and can classify bridges and overpasses as terrain, it can prevent many errors that may occur if other DTM algorithms were embedded in our algorithm Song & Jung (2022). Nevertheless, the largest portion of our error was associated with its underlying DTM. Our algorithm extracts building candidates with a height threshold (HT) based on the NDHM, which is the subtraction between DTM and DSM. This is why the accuracy and the property of DTM significantly affect the extraction of building candidates.

Although the DTM generation algorithm of Song & Jung (2022) could prevent errors from bridges and overpasses, it was not able to perfectly remove those errors. Particularly, the vast majority of errors occur at the edge of the LiDAR tile (the geographic boundaries of each LiDAR data file). This is due to the limitation of the DTM generation algorithm used in this paper whose key assumption is that small, non-rectangular areas enclosed by a certain level of a steep slope are non-grounds (please refer to Song & Jung (2022) for the detailed description). Also, as the DTM method used in this paper classifies connected components, which have smooth slopes in DSM, into a ground class, some disconnected terrain can be classified into a non-ground class.

Figure 19 provides some examples of the error caused by artifacts of DTM. The red dashed line delineates the boundary of LiDAR tiles. The first row of Figure 19 shows the region where four different LiDAR tiles are adjacent to each other. Since the bridge in the lower-left LiDAR tile was disconnected, the bridge was classified as a non-ground object by the DTM algorithm, and as a result, the disconnected part was classified as a building in our algorithm. The second row of Figure 19 shows another example of an error caused by a DTM error occurring at the edge of the LiDAR tiles. Small disconnected lands near the shoreline were classified as buildings. The third row of Figure 19 shows an example where the ground was enclosed by the building and the edge of the input LiDAR tiles. As the ground was also disconnected, the ground was classified as a building. The fourth row in Figure 19 shows an example of a suspension bridge. As pylons of the suspension bridge disconnected the two ends of the bridge, the middle part of the bridge was classified as a building. The fifth row of Figure 19 shows an example that a large pile of sand was classified as a building. This error can happen near quarries or cement factories as sand piles can be classified as a non-ground object in the DTM algorithm.

As described in Song & Jung (2022), most of the DTM errors occurring at the edge of the LiDAR tiles can be prevented by simply using the larger extent of input for data processing. However, when the larger extent of data is not available, parameter tuning of DTM (Song & Jung, 2022) or using other DTM methods (Chen et al., 2017; Zhang et al., 2016) could be considered as well. Also, if dividing the full data into multiple tiles is needed due to the limited computational resources, it is also a good way to make overlaps among the tiles and use only the central part of each tile.

### 4.3.4 Deformation during the morphological filtering

Our algorithm extracts buildings from among building candidates that contain both buildings and trees. For the classification, we used the morphological filtering of erosion and dilation with the kernel size of  $K1$ . One problem with this filtering is that dilation after erosion may not recover the original shape of the object. In other words, the dilation is not the inverse function of the erosion. If a rectangular building's edge is not aligned with the  $X$  or  $Y$  axis, the corner can be blunted when the square-shaped kernel is used. This deformation becomes severe as  $K1$  increases.

Figure 20 illustrates a toy example of the morphological filtering process on the mockup residential buildings. The building area before and after the morphological filtering was denoted as well. If building edges are aligned with the  $X$  or  $Y$  axis perfectly, dilation after erosion can recover the original shape perfectly with the square-shaped kernel. However, if buildings are oriented out of the  $X$  or  $Y$  axis, dilation after erosion cannot recover the original shape and its area. Since most cities, particularly in the US, were designed to have a north-south orientation, the deformation after the morphological filtering can be marginal. However, if buildings are oriented out of cardinal directions, the deformation will cause more errors in the boundary of extracted building and will cause biases in its area as well.

One alternative is to use a diamond-shaped kernel. The custom diamond kernel and corresponding resultants were also provided in Figure 20. It can alleviate the deformation, but it still cannot perfectly recover the original shape. Alternatively, calculating the main orientation of all individual buildings and applying the most appropriate kernel for each of them would produce more accurate building boundaries. However, it will add a significant computational burden to the current process. Obviously, a smaller kernel would preserve the original shape better and would produce better results as long as trees and unnecessary small non-building objects can be removed. The default kernel, a square  $K1$  of 7, performed reasonably well in diverse study areas for the 0.5-meter by 0.5-meter resolution. However, to obtain better results, the classification scheme, the leaf condition, and the building orientation should be considered to find the best kernel for the given study area.

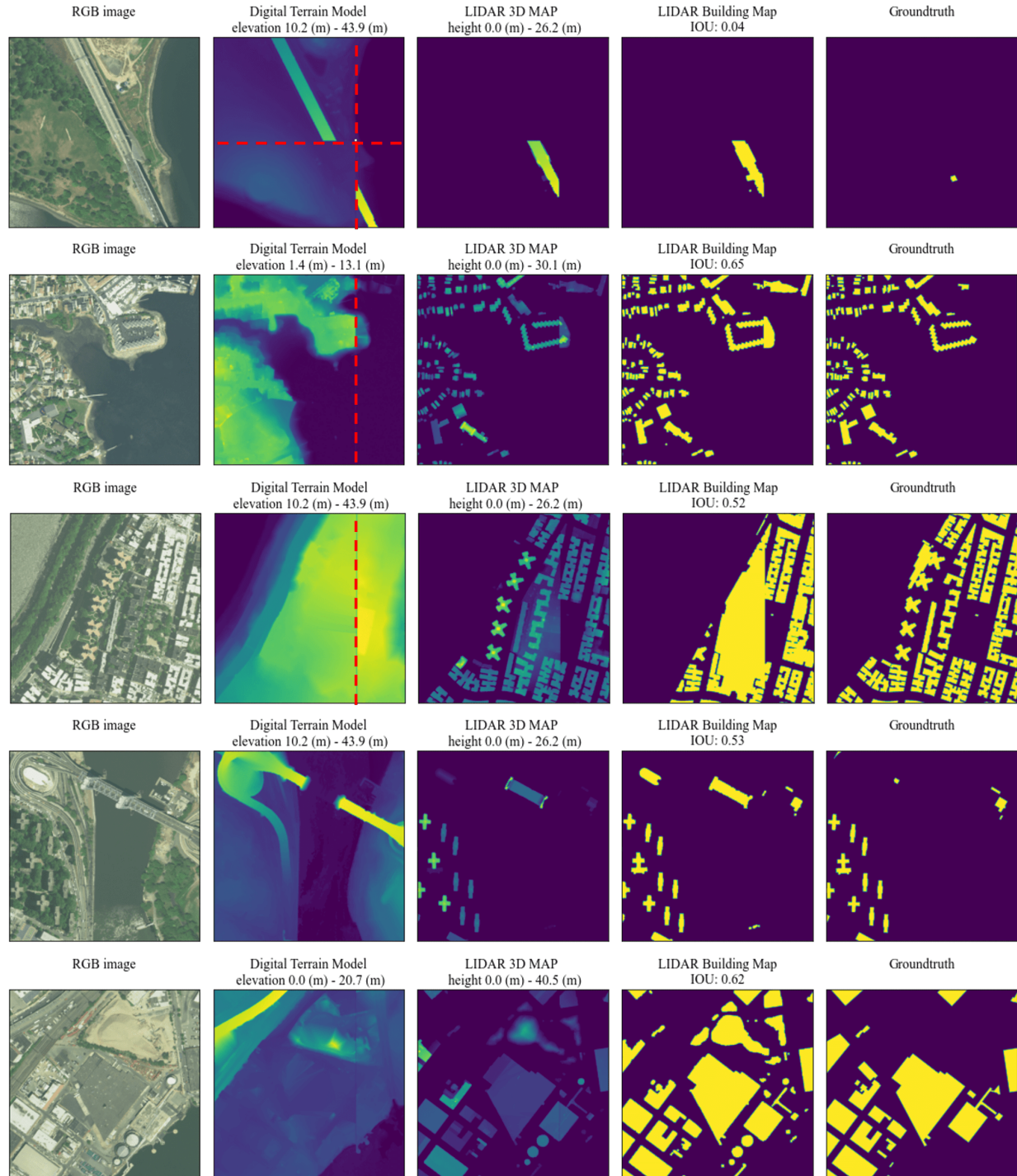


Figure 19: Commission errors caused by artifacts in DTM (The red dashed line indicates the data boundary of the LiDAR tile)



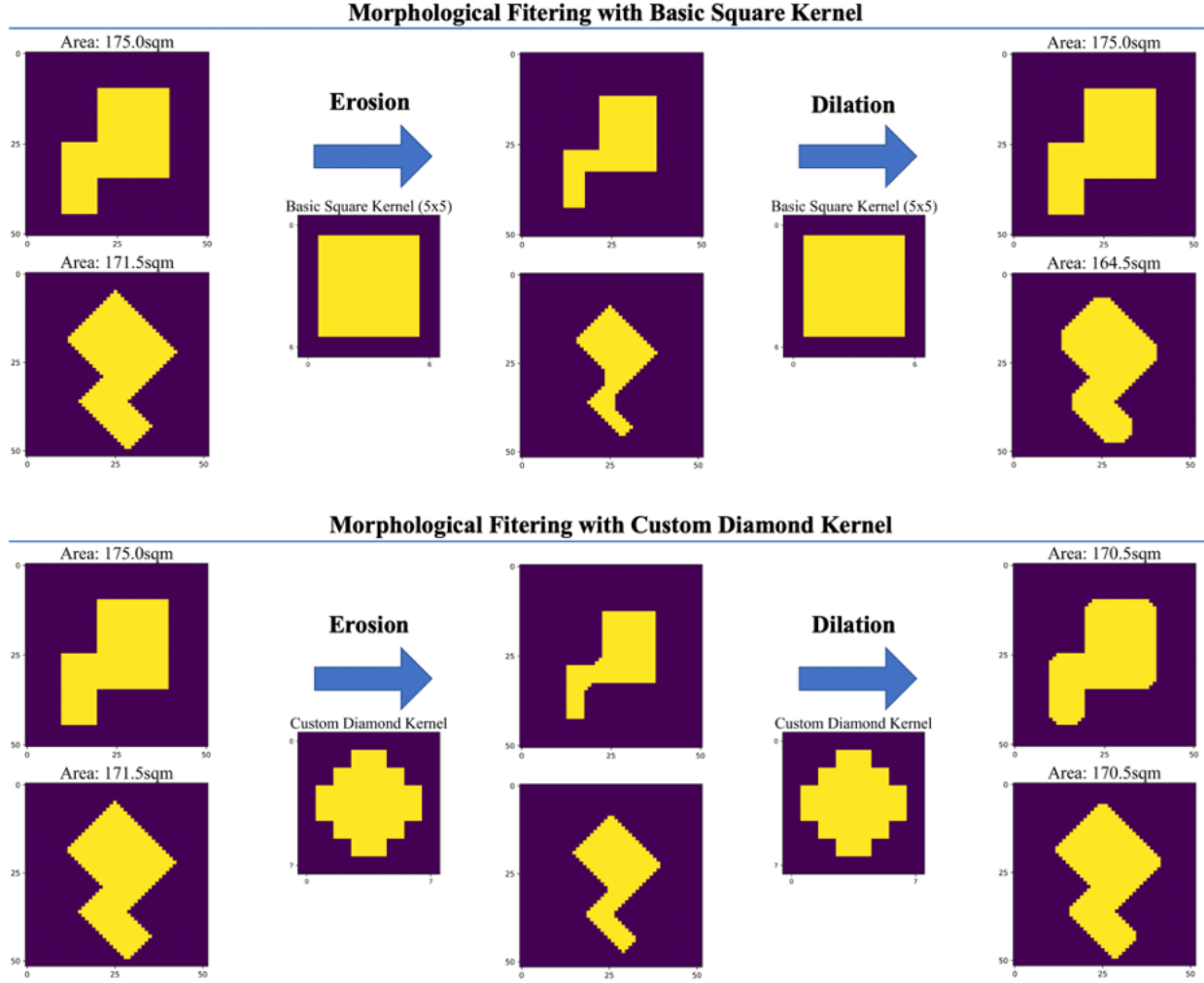


Figure 20: Examples of deformations caused by morphological filters

#### 4.3.5 Limitations in 3D building map

This study also contributes to providing an end-to-end method for generating a 3D building map from the raw LiDAR data. As long as NDHM and 2D building footprints are produced, generating a 3D building map is possible by simply masking NDHM with 2D building footprints. It produced a reliable 3D building model in most cases, but we have observed some errors near some high-rise buildings and in the residential buildings under the overhanging trees. Figure 17 in Section 4.3.1. and Figure 18 in Section 4.3.2. show examples of artifacts in 3D building models near skyscrapers and under overhanging trees, respectively. Applying a median filter for smoothing roof elevations would result in a cleaner 3D building model. However, it will add up more computations, and it may eliminate small sub-structures such as chimneys by overly regularizing the details of the roof pattern. The quality of the 3D building model is directly related to the quality of the LiDAR data, and the geometric quality assessment of the 3D building model may require more accurate reference measurement (Elberink & Vosselman, 2011). This study has a limitation in that a detailed quality assessment of 3D building models is not performed. Future works on refining a 3D building model and developing a method for assessing the quality of a 3D building model in a large-scale 3D building map are needed. Another limitation of our 3D building map lies in its low level of detail (Gröger & Plümer, 2012). Our 3D building map does not include the inside or the side of buildings. Also, the color information is not provided.

#### 4.4 Scalability for global-scale mapping

Our algorithm is designed to perform well in large-scale mapping. Our algorithm could have produced more accurate results if more sophisticated rules had been added to fit into some specific landscapes. However, as scalability was

the most important consideration of the performance, our algorithm is designed to have only simple, generalizable operations. We have mapped 2D and 3D building models of extensive, diverse areas using our method. Although not all results have been described in this paper, the mapped areas cover more than 100 regions of cities in 50 states in the US, and their accumulated areas are more than 1,000 km<sup>2</sup>. In addition, our algorithm was also applied to some uninhabited natural areas, such as national forests, deserts, and mountainous areas to investigate possible sources of error that can occur when performing the global-scale mapping. Here, we summarize some notable errors that we have observed during the mapping and discuss some important issues for global-scale building mapping in comparison with image-based building mapping.

#### 4.4.1 Potential errors

If the mapping area is too large, a complete inspection of the qualities of generated buildings will be impossible. Therefore, recognizing potential errors is very important. To explore expected outcomes and limitations in a global-scale building mapping with LiDAR, we extensively applied our algorithm to diverse areas under different conditions of data from 50 states of the US and evaluated the results qualitatively. To be specific, we checked 788 cities in the US with more than 50,000 populations and randomly selected several cities from each state. In total, we tested our algorithm in more than 100 regions from different cities where LiDAR data is available and where the landscape shows unique features. Although we did not include the detailed results for all experimented tiles in this paper, we summarize frequently occurring errors in our algorithm in Table 11 to provide information to potential users of our method and to facilitate future studies. Although there were many different types of errors and some of them cannot be completely eliminated, most errors were explainable and predictable. We argue that the explainable and predictable properties are the huge advantages of our algorithm over other deep learning-based algorithms as the user of our algorithm can better manage errors and better anticipate uncertainties that could influence subsequent analyses.

Table 11: Summary of frequently occurred errors in our algorithm

Commission error (wrongly detected as buildings)	Overhanging trees, dense trees, non-building objects (e.g., huge rock, airplane, sculpture), bridges, overpasses, etc.
Omission error (missing buildings)	Building under overhanging trees, buildings on the cliff, semi-underground buildings, etc.

#### 4.4.2 LiDAR-based mapping vs. Image-based mapping

To produce a building map with a comparable resolution to that from a high-resolution satellite image (e.g., 1-meter resolution), the point density of LiDAR data should be at least approximately 1-points/m<sup>2</sup>. This is because having 1-points/m<sup>2</sup> is the minimal requirement to have at least one measure over a 1-m<sup>2</sup> grid. It means laser scanning from an airborne platform is required. Although some missions started LiDAR mapping with a space-borne platform (Zwally et al., 2002; Markus et al., 2017; Hancock et al., 2019), the quality of LiDAR data in terms of resolution and spatial coverage is very limited. On the contrary, as lots of satellite images are available, building mapping by using existing satellite images of the target area would be cheaper than mapping with LiDAR after conducting a new ALS. Also, an ALS system would not be available to map flight restricted areas while satellite images are possible to cover anywhere on Earth.

However, we observed that the state-of-the-art of image-based building maps has lots of errors and uncertainties. In addition, the image-based method requires not only images but also training labels. Microsoft’s algorithm used millions of building labels for training the model for the US mapping<sup>3</sup>, but its product was not accurate than our algorithm. On contrary, our algorithm is an unsupervised method. It does not require any effort for the preparation of the training dataset and training. The computation is very light and all processes can be done with the CPU, which gives significant advantages in terms of scalability. Also, it can produce accurate, explainable, and predictable results. In New York City dataset, the time difference between LiDAR data and the ground-truth was around 8 years, while Microsoft’s algorithm has around 3 years gap. Despite the disadvantage of larger time discrepancy, our algorithm produced better results in general. What it suggests is that we can expect to maintain maps of better quality by using our algorithm even without more frequent surveying. It will allow mapping agencies to save on the cost of data collection. Another huge advantage is that LiDAR data is not affected by atmospheric conditions. Satellite images can provide a larger spatial coverage but having a complete cloud-free image for a large-scale area might take lots of time (Ju & Roy, 2008; Roy et al., 2021). Particularly, if a timely mapping is required for aiding disasters like earthquake (Ural et al., 2011; Anniballe et al., 2018) or hurricane (Yeom et al., 2019; Zhou et al., 2019), LiDAR-based mapping would be a better

<sup>3</sup><https://github.com/microsoft/USBuildingFootprints>

choice. Furthermore, LiDAR-based building mapping enables 3D building mapping with little additional effort. On the contrary, image-based building mapping requires a lot of costs to generate a 3D building model, and its accuracy is limited compared to that of LiDAR-based measurement in general (Widyaningrum & Gorte, 2017; Salach et al., 2018; Huang et al., 2022; Qin, 2019). With that, we argue that LiDAR-based building mapping could be a better option for scalable 2D and 3D building mapping than image-based building mapping.

## 5 Conclusion

We present an open-source LiDAR-based 2D and 3D building mapping algorithm that is suitable for large-scale mapping. This paper is the first time to evaluate the LiDAR-based building map on a large scale ( $> 550 \text{ km}^2$ ) as far as we know. Our algorithm is computationally efficient and can produce accurate and explainable results.

For the past decade, deep learning-based methods have been dominating the literature as the advancement of deep learning enables 2D building mapping with only image data. The image-based deep learning algorithm has an advantage in that image data has better availability than LiDAR data. Nevertheless, the image-based deep learning algorithm has a fundamental disadvantage in that it generally requires training procedures, and its result is hardly predictable and often not explicable. Although deep learning-based methods can obtain high accuracy in their quantitative metrics, if the user of their output cannot anticipate and understand the errors or biases that the deep model can result in, subsequent studies based on the generated building map can mislead the outcomes.

On the other hand, the results of our algorithm are explainable and predictable. This is because our algorithm is based on the very simple assumption that the building is a ground-standing object with a relatively smooth and laser-impermeable surface. Also, as the operation is fully unsupervised and very simple, all procedures are clearly visible unlike a "black box" of deep learning.

Despite our algorithm's outperforming performance, several limitations still remain. Most of the limitations can be resolved with better quality (high point density) LiDAR data. However, unclear boundaries between dense trees and small buildings, misidentification between non-building structures and buildings, deformation during morphological filtering, and errors from DTM are remaining limitations needed to be addressed in future studies. If the study area is small, adding more sophisticated rules to our algorithm may fix some errors. However, if the goal is a large-scale mapping where all outputs cannot be validated after the mapping, careful consideration is needed not to lose the generalization performance.

The source code of our algorithm will be publicly available via GitHub. Also, the 2D and 3D building maps generated from our algorithm will be released and kept updated. We hope our algorithms and our findings contribute to facilitating building mappings for various social and environmental studies and provoke future research towards 2D and 3D building mapping with airborne LiDAR data.

## References

- Anniballe, R., Noto, F., Scalia, T., Bignami, C., Stramondo, S., Chini, M., and Pierdicca, N. Earthquake damage mapping: An overall assessment of ground surveys and vhr image change detection after l'aquila 2009 earthquake. *Remote sensing of environment*, 210:166–178, 2018.
- Awrangjeb, M., Zhang, C., Fraser, C. S., et al. Building detection in complex scenes thorough effective separation of buildings from trees. *Photogrammetric Engineering & Remote Sensing*, 78(7):729–745, 2012.
- Bauranov, A. and Rakas, J. Designing airspace for urban air mobility: A review of concepts and approaches. *Progress in Aerospace Sciences*, 125:100726, 2021.
- Biljecki, F., Arroyo Ogori, K., Ledoux, H., Peters, R., and Stoter, J. Population estimation using a 3d city model: A multi-scale country-wide study in the netherlands. *PLoS one*, 11(6):e0156808, 2016a.
- Biljecki, F., Ledoux, H., Stoter, J., and Vosselman, G. The variants of an lod of a 3d building model and their influence on spatial analyses. *ISPRS Journal of Photogrammetry and Remote Sensing*, 116:42–54, 2016b.
- Bonafilia, D., Gill, J., Basu, S., and Yang, D. Building high resolution maps for humanitarian aid and development with weakly-and semi-supervised learning. In *Proceedings of the IEEE/CVF Conference on Computer Vision and Pattern Recognition Workshops*, pp. 1–9, 2019.
- Chen, S., Shi, W., Zhou, M., Zhang, M., and Chen, P. Automatic building extraction via adaptive iterative segmentation with lidar data and high spatial resolution imagery fusion. *IEEE Journal of Selected Topics in Applied Earth Observations and Remote Sensing*, 13:2081–2095, 2020.
- Chen, Z., Gao, B., and Devereux, B. State-of-the-art: Dtm generation using airborne lidar data. *Sensors*, 17(1):150, 2017.
- Cheng, L., Gong, J., Li, M., and Liu, Y. 3d building model reconstruction from multi-view aerial imagery and lidar data. *Photogrammetric Engineering & Remote Sensing*, 77(2):125–139, 2011.
- Cheng, L., Tong, L., Chen, Y., Zhang, W., Shan, J., Liu, Y., and Li, M. Integration of lidar data and optical multi-view images for 3d reconstruction of building roofs. *Optics and Lasers in Engineering*, 51(4):493–502, 2013.
- Deng, X., Yang, H. L., Makkar, N., and Lunga, D. Large scale unsupervised domain adaptation of segmentation networks with adversarial learning. In *IGARSS 2019-2019 IEEE International Geoscience and Remote Sensing Symposium*, pp. 4955–4958. IEEE, 2019.
- Domínguez, E. M., Magnard, C., Meier, E., Small, D., Schaepman, M. E., and Henke, D. A back-projection tomographic framework for vhr sar image change detection. *IEEE Transactions on Geoscience and Remote Sensing*, 57(7):4470–4484, 2019.
- Donoghue, D. N., Watt, P. J., Cox, N. J., and Wilson, J. Remote sensing of species mixtures in conifer plantations using lidar height and intensity data. *Remote Sensing of Environment*, 110(4):509–522, 2007.
- Dorn, H., Törnros, T., and Zipf, A. Quality evaluation of vgi using authoritative data—a comparison with land use data in southern germany. *ISPRS International Journal of Geo-Information*, 4(3):1657–1671, 2015.
- Ekhtari, N., Sahebi, M., Zoj, M. V., and Mohammadzadeh, A. Automatic building detection from lidar point cloud data. *The International Archive of the Photogrammetry, Remote Sensing and Spatial Information Sciences*, 37, 2008.
- Elberink, S. O. and Vosselman, G. Quality analysis on 3d building models reconstructed from airborne laser scanning data. *ISPRS Journal of Photogrammetry and Remote Sensing*, 66(2):157–165, 2011.
- Ghaffarian, S., Kerle, N., Pasolli, E., and Jokar Arsanjani, J. Post-disaster building database updating using automated deep learning: An integration of pre-disaster openstreetmap and multi-temporal satellite data. *Remote sensing*, 11(20):2427, 2019.
- Gröger, G. and Plümer, L. Citygml—interoperable semantic 3d city models. *ISPRS Journal of Photogrammetry and Remote Sensing*, 71:12–33, 2012.
- Han, J.-Y., Chen, Y.-C., and Li, S.-Y. Utilising high-fidelity 3d building model for analysing the rooftop solar photovoltaic potential in urban areas. *Solar Energy*, 235:187–199, 2022.
- Hancock, S., Armston, J., Hofton, M., Sun, X., Tang, H., Duncanson, L. I., Kellner, J. R., and Dubayah, R. The gedi simulator: A large-footprint waveform lidar simulator for calibration and validation of spaceborne missions. *Earth and Space Science*, 6(2):294–310, 2019.
- Herbert, G. and Chen, X. A comparison of usefulness of 2d and 3d representations of urban planning. *Cartography and Geographic Information Science*, 42(1):22–32, 2015.
- Herfort, B., Lautenbach, S., Porto de Albuquerque, J., Anderson, J., and Zipf, A. The evolution of humanitarian mapping within the openstreetmap community. *Scientific reports*, 11(1):1–15, 2021.

- Heris, M. P., Foks, N. L., Bagstad, K. J., Troy, A., and Ancona, Z. H. A rasterized building footprint dataset for the united states. *Scientific data*, 7(1):1–10, 2020.
- Hong, J.-W., Hong, J., Kwon, E. E., and Yoon, D. Temporal dynamics of urban heat island correlated with the socio-economic development over the past half-century in seoul, korea. *Environmental Pollution*, 254:112934, 2019.
- Hosseinpour, H., Samadzadegan, F., and Javan, F. D. Cmgfnet: A deep cross-modal gated fusion network for building extraction from very high-resolution remote sensing images. *ISPRS journal of photogrammetry and remote sensing*, 184:96–115, 2022.
- Hu, Z., Hou, Y., Tao, P., and Shan, J. Imgtr: Image-triangle based multi-view 3d reconstruction for urban scenes. *ISPRS Journal of Photogrammetry and Remote Sensing*, 181:191–204, 2021.
- Huang, D., Tang, Y., and Qin, R. An evaluation of planetscope images for 3d reconstruction and change detection—experimental validations with case studies. *GIScience & Remote Sensing*, 59(1):744–761, 2022.
- Huang, J., Zhang, X., Xin, Q., Sun, Y., and Zhang, P. Automatic building extraction from high-resolution aerial images and lidar data using gated residual refinement network. *ISPRS journal of photogrammetry and remote sensing*, 151: 91–105, 2019.
- Huang, X. and Wang, Y. Investigating the effects of 3d urban morphology on the surface urban heat island effect in urban functional zones by using high-resolution remote sensing data: A case study of wuhan, central china. *ISPRS Journal of Photogrammetry and Remote Sensing*, 152:119–131, 2019.
- Hyypä, J., Kelle, O., Lehtikoinen, M., and Inkinen, M. A segmentation-based method to retrieve stem volume estimates from 3-d tree height models produced by laser scanners. *IEEE Transactions on geoscience and remote sensing*, 39(5):969–975, 2001.
- Ji, S., Wei, S., and Lu, M. Fully convolutional networks for multisource building extraction from an open aerial and satellite imagery data set. *IEEE Transactions on Geoscience and Remote Sensing*, 57(1):574–586, 2018.
- Jokar Arsanjani, J., Mooney, P., Zipf, A., and Schauss, A. Quality assessment of the contributed land use information from openstreetmap versus authoritative datasets. In *OpenStreetMap in GIScience*, pp. 37–58. Springer, 2015.
- Ju, J. and Roy, D. P. The availability of cloud-free landsat etm+ data over the conterminous united states and globally. *Remote Sensing of Environment*, 112(3):1196–1211, 2008.
- Jung, J., Pekin, B. K., and Pijanowski, B. C. Mapping open space in an old-growth, secondary-growth, and selectively-logged tropical rainforest using discrete return lidar. *IEEE Journal of Selected Topics in Applied Earth Observations and Remote Sensing*, 6(6):2453–2461, 2013.
- Jung, J., Pasolli, E., Prasad, S., Tilton, J. C., and Crawford, M. M. A framework for land cover classification using discrete return lidar data: Adopting pseudo-waveform and hierarchical segmentation. *IEEE Journal of Selected Topics in Applied Earth Observations and Remote Sensing*, 7(2):491–502, 2014.
- Kaiser, P., Wegner, J. D., Lucchi, A., Jaggi, M., Hofmann, T., and Schindler, K. Learning aerial image segmentation from online maps. *IEEE Transactions on Geoscience and Remote Sensing*, 55(11):6054–6068, 2017.
- Kim, N. and Yoon, Y. Regionalization for urban air mobility application with analyses of 3d urban space and geodemography in san francisco and new york. *Procedia Computer Science*, 184:388–395, 2021.
- Lehner, H. and Dorffner, L. Digital geotwin vienna: towards a digital twin city as geodata hub, 2020.
- Li, M., Koks, E., Taubenböck, H., and van Vliet, J. Continental-scale mapping and analysis of 3d building structure. *Remote Sensing of Environment*, 245:111859, 2020.
- Ma, L., Liu, Y., Zhang, X., Ye, Y., Yin, G., and Johnson, B. A. Deep learning in remote sensing applications: A meta-analysis and review. *ISPRS journal of photogrammetry and remote sensing*, 152:166–177, 2019.
- Macchione, F., Costabile, P., Costanzo, C., and De Santis, R. Moving to 3-d flood hazard maps for enhancing risk communication. *Environmental modelling & software*, 111:510–522, 2019.
- Maggiori, E., Tarabalka, Y., Charpiat, G., and Alliez, P. Convolutional neural networks for large-scale remote-sensing image classification. *IEEE Transactions on geoscience and remote sensing*, 55(2):645–657, 2016.
- Mahabir, R., Stefanidis, A., Croitoru, A., Crooks, A. T., and Agouris, P. Authoritative and volunteered geographical information in a developing country: A comparative case study of road datasets in nairobi, kenya. *ISPRS International Journal of Geo-Information*, 6(1):24, 2017.
- Makkar, N., Yang, L., and Prasad, S. Adversarial learning based discriminative domain adaptation for geospatial image analysis. *IEEE Journal of Selected Topics in Applied Earth Observations and Remote Sensing*, 15:150–162, 2021.
- Maltezos, E., Doulamis, A., Doulamis, N., and Ioannidis, C. Building extraction from lidar data applying deep convolutional neural networks. *IEEE Geoscience and Remote Sensing Letters*, 16(1):155–159, 2018.

- Markus, T., Neumann, T., Martino, A., Abdalati, W., Brunt, K., Csatho, B., Farrell, S., Fricker, H., Gardner, A., Harding, D., et al. The ice, cloud, and land elevation satellite-2 (icesat-2): science requirements, concept, and implementation. *Remote sensing of environment*, 190:260–273, 2017.
- Moreno-Torres, J. G., Raeder, T., Alaiz-Rodríguez, R., Chawla, N. V., and Herrera, F. A unifying view on dataset shift in classification. *Pattern recognition*, 45(1):521–530, 2012.
- Morgan, M. and Habib, A. Interpolation of lidar data and automatic building extraction. In *ACSM-ASPRS Annual conference proceedings*, pp. 432–441. Citeseer, 2002.
- Oh, S., Jung, J., Shao, G., Shao, G., Gallion, J., and Fei, S. High-resolution canopy height model generation and validation using usgs 3dep lidar data in indiana, usa. *Remote Sensing*, 14(4):935, 2022.
- Ojogbane, S. S., Mansor, S., Kalantar, B., Khuzaimah, Z. B., Shafri, H. Z. M., and Ueda, N. Automated building detection from airborne lidar and very high-resolution aerial imagery with deep neural network. *Remote Sensing*, 13(23):4803, 2021.
- Park, Y., Guldmann, J.-M., and Liu, D. Impacts of tree and building shades on the urban heat island: Combining remote sensing, 3d digital city and spatial regression approaches. *Computers, Environment and Urban Systems*, 88:101655, 2021.
- Qin, R. A critical analysis of satellite stereo pairs for digital surface model generation and a matching quality prediction model. *ISPRS Journal of Photogrammetry and Remote Sensing*, 154:139–150, 2019.
- Rottensteiner, F., Sohn, G., Jung, J., Gerke, M., Baillard, C., Benitez, S., and Breitkopf, U. The isprs benchmark on urban object classification and 3d building reconstruction. *ISPRS Annals of the Photogrammetry, Remote Sensing and Spatial Information Sciences I-3 (2012), Nr. 1*, 1(1):293–298, 2012.
- Rottensteiner, F., Sohn, G., Gerke, M., Wegner, J. D., Breitkopf, U., and Jung, J. Results of the isprs benchmark on urban object detection and 3d building reconstruction. *ISPRS journal of photogrammetry and remote sensing*, 93: 256–271, 2014.
- Roy, D. P., Huang, H., Houborg, R., and Martins, V. S. A global analysis of the temporal availability of planetscope high spatial resolution multi-spectral imagery. *Remote Sensing of Environment*, 264:112586, 2021.
- Salach, A., Bakula, K., Pilarska, M., Ostrowski, W., Górski, K., and Kurczyński, Z. Accuracy assessment of point clouds from lidar and dense image matching acquired using the uav platform for dtm creation. *ISPRS International Journal of Geo-Information*, 7(9):342, 2018.
- Song, H. and Jung, J. A new explainable dtm generation algorithm with airborne lidar data: grounds are smoothly connected eventually. *arXiv preprint arXiv:2208.11243*, 2022.
- Tan, M. and Le, Q. Efficientnet: Rethinking model scaling for convolutional neural networks. In *International conference on machine learning*, pp. 6105–6114. PMLR, 2019.
- Ural, S., Hussain, E., Kim, K., Fu, C.-S., and Shan, J. Building extraction and rubble mapping for city port-au-prince post-2010 earthquake with geoeye-1 imagery and lidar data. *Photogrammetric Engineering & Remote Sensing*, 77(10):1011–1023, 2011.
- Van Etten, A., Lindenbaum, D., and Bacastow, T. M. Spacenet: A remote sensing dataset and challenge series. *arXiv preprint arXiv:1807.01232*, 2018.
- Vargas-Munoz, J. E., Srivastava, S., Tuia, D., and Falcao, A. X. Openstreetmap: Challenges and opportunities in machine learning and remote sensing. *IEEE Geoscience and Remote Sensing Magazine*, 9(1):184–199, 2020.
- Wang, S., Tian, Y., Zhou, Y., Liu, W., and Lin, C. Fine-scale population estimation by 3d reconstruction of urban residential buildings. *Sensors*, 16(10):1755, 2016.
- White, G., Zink, A., Codecá, L., and Clarke, S. A digital twin smart city for citizen feedback. *Cities*, 110:103064, 2021.
- Widyaningrum, E. and Gorte, B. Comprehensive comparison of two image-based point clouds from aerial photos with airborne lidar for large-scale mapping. *Int. Arch. Photogramm. Remote Sens. Spat. Inf. Sci.*, 42:557–565, 2017.
- Williams, T. K.-A., Wei, T., and Zhu, X. Mapping urban slum settlements using very high-resolution imagery and land boundary data. *IEEE Journal of Selected Topics in Applied Earth Observations and Remote Sensing*, 13:166–177, 2019.
- Wu, S.-s., Qiu, X., and Wang, L. Population estimation methods in gis and remote sensing: A review. *GIScience & Remote Sensing*, 42(1):80–96, 2005.
- Wurm, M., Stark, T., Zhu, X. X., Weigand, M., and Taubenböck, H. Semantic segmentation of slums in satellite images using transfer learning on fully convolutional neural networks. *ISPRS journal of photogrammetry and remote sensing*, 150:59–69, 2019.

- Yan, Y., Gao, F., Deng, S., and Su, N. A hierarchical building segmentation in digital surface models for 3d reconstruction. *Sensors*, 17(2):222, 2017.
- Yang, H. L., Yuan, J., Lunga, D., Laverdiere, M., Rose, A., and Bhaduri, B. Building extraction at scale using convolutional neural network: Mapping of the united states. *IEEE Journal of Selected Topics in Applied Earth Observations and Remote Sensing*, 11(8):2600–2614, 2018.
- Yeom, J., Han, Y., Chang, A., and Jung, J. Hurricane building damage assessment using post-disaster uav data. In *IGARSS 2019-2019 IEEE International Geoscience and Remote Sensing Symposium*, pp. 9867–9870. IEEE, 2019.
- Yu, X., Liu, Y., Zhang, Z., and Xiao, R. Influences of buildings on urban heat island based on 3d landscape metrics: An investigation of china’s 30 megacities at micro grid-cell scale and macro city scale. *Landscape Ecology*, 36(9): 2743–2762, 2021.
- Yuan, Q., Shafri, H. Z. M., Alias, A. H., and Hashim, S. J. b. Multiscale semantic feature optimization and fusion network for building extraction using high-resolution aerial images and lidar data. *Remote Sensing*, 13(13):2473, 2021a.
- Yuan, X., Shi, J., and Gu, L. A review of deep learning methods for semantic segmentation of remote sensing imagery. *Expert Systems with Applications*, 169:114417, 2021b.
- Zhang, W., Qi, J., Wan, P., Wang, H., Xie, D., Wang, X., and Yan, G. An easy-to-use airborne lidar data filtering method based on cloth simulation. *Remote sensing*, 8(6):501, 2016.
- Zhao, T. Object-based urban building footprint extraction and 3d building reconstruction from airborne lidar data. 2013.
- Zhao, Z., Duan, Y., Zhang, Y., and Cao, R. Extracting buildings from and regularizing boundaries in airborne lidar data using connected operators. *International Journal of Remote Sensing*, 37(4):889–912, 2016.
- Zhou, Z., Gong, J., and Hu, X. Community-scale multi-level post-hurricane damage assessment of residential buildings using multi-temporal airborne lidar data. *Automation in Construction*, 98:30–45, 2019.
- Zhu, X. X., Tuia, D., Mou, L., Xia, G.-S., Zhang, L., Xu, F., and Fraundorfer, F. Deep learning in remote sensing: A comprehensive review and list of resources. *IEEE Geoscience and Remote Sensing Magazine*, 5(4):8–36, 2017.
- Zhu, Z., Zhou, Y., Seto, K. C., Stokes, E. C., Deng, C., Pickett, S. T., and Taubenböck, H. Understanding an urbanizing planet: Strategic directions for remote sensing. *Remote Sensing of Environment*, 228:164–182, 2019.
- Zwally, H. J., Schutz, B., Abdalati, W., Abshire, J., Bentley, C., Brenner, A., Bufton, J., Dezio, J., Hancock, D., Harding, D., et al. Icesat’s laser measurements of polar ice, atmosphere, ocean, and land. *Journal of Geodynamics*, 34(3-4): 405–445, 2002.